Two-phase vertical downward flow in plate heat exchangers
Flow patterns and condensation mechanisms

Tao, Xuan; Nuijten, Menno P.; Infante Ferreira, Carlos A.

DOI
10.1016/j.ijrefrig.2017.10.008

Publication date
2018

Document Version
Accepted author manuscript

Published in
International Journal of Refrigeration

Two-phase vertical downward flow in plate heat exchangers: flow patterns and condensation mechanisms

X. Tao[a], M. P. Nuijten[a], C. A. Infante Ferreira[a*]

[a)] Process and Energy Laboratory, Delft University of Technology, Leeghwaterstraat 39, 2628 CB, Delft, The Netherlands.

E-mail: X.Tao@tudelft.nl mennonuijten@gmail.com c.a.infanteferreira@tudelft.nl

Abstract

This study presents a literature review of work related to the two-phase flow patterns of vertical downward flow in plate heat exchangers with corrugated chevron plates. An understanding of these flow patterns is crucial for developing accurate models of plate heat exchangers functioning as condensers or absorbers. Flow pattern maps of the previous studies are combined and translated to dimensionless forms. One of the proposed flow pattern maps is based on Re_L versus $Fr_{TP,hor} / \Lambda^{0.5}$ and performs better than other representations. This map is compared with the map of tubes and shows general agreements in terms of the pattern positions, but the separating lines between flow patterns fit poorly. Influencing factors of condensation mechanisms are presented, among which mass flux and vapor quality are dominant. The preferred flow pattern map explains the transition of condensation mechanisms qualitatively when variations of mass flux and vapor quality are considered. Recommendations are given to come to more uniform flow pattern maps in plate heat exchangers with chevron corrugations.

Keywords: Two-phase flow, vertical downward flow, flow patterns, plate heat exchangers, condensation mechanisms, flow visualization

[*] *Corresponding author's e-mail address: c.a.infanteferreira@tudelft.nl*

Nomenclature

Symbols

A	Heat transfer area	[m^2]
A_f	Flow passage area	[m^2]
$\hat{a}$	Corrugation amplitude	[m]
Bd	Bond number	[-]
Bo	Boiling number	[-]
d	Diameter of tubes	[m]
d_e	Equivalent diameter	[m]
d_g	Channel gap	[m]
d_h	Hydraulic diameter	[m]
d_p	Plate thickness	[m]
f	Friction factor	[-]
Fr	Froude number	[-]
g	Gravitational constant	[ms^{-2}]
G	Mass flux	[$kgm^{-2}s^{-1}$]
h	Enthalpy	[Jkg^{-1}]
j_G	Dimensionless gas velocity Eq. (16)	[-]
L	Overall plate length	[m]
L_p	Port-to-port plate length	[m]
Nu	Nusselt number	[-]
p	Corrugation pitch	[m]
p_{cp}	Compressed plate pitch	[m]
P	Pressure	[Pa]
Pr	Prandtl number	[-]
$\dot{q}$	Heat flux	[Wm^{-2}]
R_v	Gas-to-liquid volume ratio	[-]
Re	Reynolds number	[-]
T	Temperature	[K]
v	Superficial velocity	[ms^{-1}]
$\dot{V}$	Volumetric flow rate	[m^3s^{-1}]
W	Overall plate width	[m]
W_p	In gasket plate width	[m]
We	Weber number	[-]
x	Vapor quality	[-]

Greek symbols

α	Heat transfer coefficient	[$Wm^{-2}K^{-1}$]
β	Chevron angle to flow direction	[°]
β_{flow}	Chevron angle perpendicular to flow	[°]
γ	Corrugation aspect ratio	[-]
Δ	Difference	[-]
ϕ	Enlargement factor	[-]
δ	Parameter defined in Eq. (33)	[-]
ζ	Parameter defined in Eq. (37)	[-]
λ	Thermal conductivity	[$Wm^{-1}K^{-1}$]
Λ	Property modifying parameter	[-]
Λ_{wave}	Corrugation wavelength	[m]
Ω	Wave number	[-]
μ	Dynamic viscosity	[Pas]
ρ	Density	[kgm^{-3}]
σ	Surface tension	[Nm^{-1}]

Subscripts

0	Basic
av	*Averaged*
cc	Convective condensation
cr	Critical conditions
eq	Equivalent
G	Gas
gc	Gravity-controlled condensation
hor	Horizontal
L	Liquid
LG	Latent liquid to vapor
LO	Liquid only
p	Plate
sat	At saturation conditions
sup	Superheating
TP	Two-phase
ver	Vertical
W	Water
wall	At wall conditions

1. Introduction

Since their discovery more than 90 years ago, plate heat exchangers (PHEs) have been used in industry and for scientific research (Thulukkanam, 2013). Countless studies report on the superior performance of PHEs, in relation to favorable heat transfer coefficients (HTCs), liquid holdup, residence time, fluid distribution, temperature approach, compactness and general thermal effectiveness (Thulukkanam, 2013).

PHEs have recently been identified to be suitable for applications with phase change, such as evaporators, condensers and absorbers (Abu-Khader, 2012; Jung et al., 2014; Hu et al., 2015; Longo et al., 2015; Wang and Infante Ferreira, 2017). Experimental results show promising performance, but the fluid dynamics, heat and mass transfer of two-phase flow are not fully understood, which have been indicated for decades and remain addressed (Dović et al., 2009; Tsai et al., 2009; Nilpueng and Wongwises, 2010; Freund and Kabelac, 2010; Abu-Khader, 2012; Mancin et al., 2012a; Hayes et al., 2012; Le Lostec et al., 2013). Watson et al. (1960) suggested that fluid dynamics has a significant influence on the heat and mass transfer and pressure drop.

Amalfi et al. (2016a) reviewed the experiments and prediction methods of flow boiling (for both local and overall HTCs) and two-phase pressure drop (including both adiabatic and diabatic studies) within PHEs. The authors adopted the flow pattern studies of Tribbe and Müller-Steinhagen (2001b), and concluded that flow pattern effects have not yet been included in heat transfer and pressure drop prediction. Thus a deeper understanding is required. Amalfi et al. (2016b) collected 1903 heat transfer and 1513 frictional pressure drop experimental data of flow boiling in PHEs from independent researchers, and then applied non-dimensional parameters to capture the physical mechanisms of two-phase flow and to statistically process the databank. Their proposed heat transfer and pressure drop correlations predict the experimental results better than any other compared correlation (Amalfi et al., 2016b). It is expected that including flow patterns will improve the prediction methods.

Eldeeb et al. (2016) considered not only boiling but also condensation in PHEs, and reviewed the correlations of heat transfer and pressure drop. The results between studies differ significantly. The authors also suggested that for both boiling and condensation the local flow patterns play a non-negligible role.

The focus of this paper is on the flow patterns for two-phase vertical downward flow in PHEs. This flow direction corresponds to most condensers and many absorbers. Despite the importance of this topic, only limited work has been performed (Tribbe and Müller-

Steinhagen, 2001b; Vlasogiannis et al., 2002; Nilpueng and Wongwises, 2010; Winkelmann, 2010; Grabenstein and Kabelac, 2012; Grabenstein et al., 2017). Flow pattern maps for these flow patterns are developed and compared with corresponding maps for two-phase flow in tubes. Condensation mechanisms are discussed and a qualitative comparison between flow patterns and condensation regimes is made. Furthermore, recommendations are provided for future work.

Apart from introduction and conclusion, this paper is divided into six sections. Section 2 describes primary geometric structure of PHE. Section 3 focuses on the transition of condensation mechanisms and its influencing factors. In Section 4 the flow patterns are characterized. Also the original flow pattern data are summarized in flow pattern maps using v_G versus v_L and x versus G. Determining parameters of flow patterns are listed in Section 5 for the development of combined flow pattern maps in Section 6. Additionally, Section 6 compares condensation mechanisms with flow patterns, and validates the presented flow pattern map with the maps of tubes. The deviation of separating lines is also analysed. Accordingly, recommendations are given in Section 7 to improve the applicability of the flow pattern maps.

2. Geometric characteristics

This section gives the main geometric parameters of PHEs and their relations. A PHE consists of multiple stacked plates. However, for visualization studies, two plates are usually used to observe the flow in a single channel. One of the plates is made of transparent material, while the other is metal alloy (such as stainless-steel). Figs. 1-3 summarize the general geometry.

The overall geometric parameters are the overall plate width, W, the in gasket plate width, W_p, the overall plate length, L, and the port-to-port length, L_p, as given in Fig. 1. The basic heat transfer area of the plate, A_0, is the product of W_p and L_p. The effective heat transfer area, A_p, is obtained by multiplying A_0 with an area enlargement factor, ϕ, which is the ratio of the wavy plate surface to its plane projection. This factor depends on the corrugation characteristics and will be introduced in the following paragraphs.

<figure 1>

<figure 2>

<figure 3>

The area enclosed by the dash line of Fig. 1 is further described in Fig. 2. The plate contains corrugations which are approximately sinusoidal. The chevron angle, β, is the angle between the corrugation and the main flow direction, while β_{flow} is the chevron angle perpendicular to the flow direction. In this paper, chevron angle indicates the former. The corrugation pitch, *p,* is the corrugation length in the main flow direction, and the wavelength, Λ_{wave}, is the corrugation length in the direction of the corrugation pattern. Both are related through the chevron angle, β. The corrugations are mirrored in the center plane of the plate, making the pattern symmetrical. Two plates are placed with opposite pattern directions and contact at the top of the corrugations.

Fig. 3 presents a sinusoidal corrugation and is a detail of Fig. 2. The average spacing between the plates is the channel gap, d_g, sometimes referred to pressing depth, and is defined as twice the amplitude, $\hat{a}$. The compressed plate pitch, p_{cp}, is the sum of the channel gap and the plate thickness, d_p, and is the effective depth added to the heat exchanger. Their relationships are indicated in Eq. (1), which is the definition of the wave number, Ω. For a sinusoidal corrugation, the area enlargement factor is approximately a function of the wave number, Ω, which is given in Eq. (2) (Stephan et al. 2010).

$$\Omega = \frac{\pi(p_{cp} - d_p)}{\Lambda_{wave}} = \frac{\pi d_g}{\Lambda_{wave}} = \frac{2\pi\hat{a}}{\Lambda_{wave}} \tag{1}$$

$$\phi(\Omega) \approx \frac{1}{6}\left[1 + \sqrt{1+\Omega^2} + 4\sqrt{1+\frac{\Omega^2}{2}} \right] \tag{2}$$

The corrugation aspect ratio, γ, is twice the ratio of the channel gap to the wavelength, which indicates the degree of surface corrugation (Amalfi et al., 2016a; Muley and Manglik, 1999). It is sometimes regarded as four times the ratio (Metwally and Manglik, 2004). This paper adopts the former definition as given in Eq.(3).

$$\gamma = \frac{4\hat{a}}{\Lambda_{wave}} = \frac{2d_g}{\Lambda_{wave}} \tag{3}$$

The hydraulic diameter, d_h, and the equivalent diameter, d_e, are given in Eqs. (4)-(5). (Stephan et al., 2010; Amalfi et al., 2016a):

$$d_h = \frac{4\hat{a}}{\phi} = \frac{2d_g}{\phi} \tag{4}$$

$$d_e = 4\hat{a} = 2d_g \tag{5}$$

It is expected that the detailed geometric parameters have direct effects on two-phase flow, namely, the corrugation pitch, p, the corrugation amplitude, $\hat{a}$, and the chevron angle, β. Han et al. (2003) instead used the corrugation wavelength, Λ_{wave}, the hydraulic diameter, d_h, and the chevron angle, β_{flow}. These three parameters can be calculated from p, $\hat{a}$ and β.

3. Mechanisms of condensation

This section presents the transition of condensation mechanisms, which is affected by a series of factors. The heat transfer performance is sensitive to condensation mechanisms while the pressure drop is less influenced. It is widely accepted that condensation within PHEs can be classified as gravity-controlled condensation or convection-controlled condensation. Different concepts are utilized to describe the two regimes. Gravity-controlled condensation is also known as laminar falling film or laminar film condensation. Convective condensation or forced convection condensation is referred to as turbulent, shear dominated condensation. In this regime interfacial shear has dominant effects. There can be a transition regime where both gravity and shear are non-negligible. In gravity controlled regime, HTCs decrease with increasing mass flux, or stay almost constant if turbulence plays a role. In convective condensation, HTCs are generally reported to increase with mass flux. Mancin et al. (2013) distinguished condensation into a temperature driving force dependent regime and a temperature driving force independent regime, which are equivalent to gravity-controlled condensation and convective condensation. The influencing factors will be discussed separately in the next sections.

3.1 Mass flux, *G*

Longo (2010a / b) experimentally studied the effects of mass flux on the condensation HTCs for HFCs (R236fa, R134a and R410A) and hydrocarbons (R600a, R290 and R1270). For all the investigated refrigerants, at small mass flux the HTCs are mass flux independent, while at

larger mass flux the HTCs increase with mass flux. The transition takes place at about 20 $kg \cdot m^{-2} \cdot s^{-1}$ for HFCs and 16.5 $kg \cdot m^{-2} \cdot s^{-1}$ for hydrocarbons. Mancin et al. (2012a) analysed the condensation of R407C and R410A in a brazed PHE. For the same inlet superheating and outlet vapor quality the heat transfer coefficient of R407C is practically constant when the mass flux increases from 15 to 20 $kg \cdot m^{-2} \cdot s^{-1}$, and increases with mass flux doubling from 20 to 40 $kg \cdot m^{-2} \cdot s^{-1}$. For R410A the HTC keeps growing in the range of 15 to 40 $kg \cdot m^{-2} \cdot s^{-1}$, indicating a smaller transition mass flux. However, later experiments of Mancin et al. (2012b) showed that R410A had similar transition mass fluxes as R407C.

Sarraf et al. (2015a) investigated the condensation of saturated pentane in PHEs with mass fluxes in the range of 9 to 30 $kg \cdot m^{-2} \cdot s^{-1}$. Infrared thermography was utilized for local measurements of the thermo-hydraulic characteristics. The HTCs decrease with decreasing vapor quality. The HTCs decrease with increasing mass flux at first, and then keep almost constant for larger mass fluxes. The transition mass flux is similar to Longo (2010a / b): 15 $kg \cdot m^{-2} \cdot s^{-1}$.

The equivalent Reynolds number for two-phase flow, Re_{eq}, is given in the study by Akers et al. (1958):

$$Re_{eq} = G[(1-x) + x(\rho_L / \rho_G)^{1/2}]d_h / \mu_L \tag{6}$$

When the equivalent Reynolds number is used to classify the flow, the transition values of Longo (2010a / b) are 1650 for both types of refrigerants. At small mass flux, condensation is mainly governed by gravity. Interfacial shear has a negligible effect on the condensate flow. In this regime Nusselt's (1916) derivation for laminar film condensation on a vertical wall gives a good approximation of the condensation process. According to Nusselt's derivation, an increase of the mass flux leads to a reduction of the HTC. However, this was not verified during Longo's (2010a / b) experiments for which the HTC remained constant as the mass flux increased. The author attributed this to the accuracy of experiments and the fact that turbulence cannot be completely eliminated at small mass flux. Thonon and Bontemps (2002) investigated the condensation of hydrocarbons including pentane, butane, propane, as well as mixtures of butane and propane. In their laminar falling film experiments, an increase in mass flux results in a decrease of the HTC.

Longo et al. (2015) adopted Nusselt's (1916) derivation for saturated vapor condensation in the gravity-controlled regime within PHEs, and predicted the authors' own experimental HTCs with reasonable accuracy. According to Longo et al. (2015), Nusselt's derivation agrees with experimental results from different sources (Nusselt, 1916).

$$Nu_{gc} = 0.943\left[\frac{g\rho_L(\rho_L-\rho_G)L_p^3\Delta h_{LG}}{\mu_L\lambda_L\Delta T}\right]^{0.25} \quad (7)$$

Where $\Delta T = T_{sat} - T_{wall}$ is the temperature difference between the saturated refrigerant and the wall. Δh_{LG} is the latent heat of the saturated vapor, and is added with the sensible heat for de-superheating the vapor in superheated conditions.

Forced convective condensation appears at larger mass flux and is mainly governed by interfacial shear. The interfacial shear reduces the thickness of the condensate film and promotes turbulence in the condensate film. Additionally interfacial shear modifies the fluid distribution in the condensation region (Sarraf et al., 2015a, 2016). An increase in mass flux leads to an increase of the HTC. Also in the experiments of Thonon and Bontemps (2002) turbulent effects arise at larger mass fluxes and the HTCs increase with mass flux. Sarraf et al. (2015a, 2016) reported that, after the transition, the HTCs remain almost constant for increasing mass fluxes. The constant regime of HTCs suggests the combined effects of gravity and interfacial shear. The trend in this regime is different from Longo's (2010a) and Thonon and Bontemps' (2002).

Mass flux is the main contributor to the transition from gravity-controlled condensation to convective condensation. The exact transition mass flux values are different among several researches and are affected by refrigerant properties and PHE geometries.

Yan et al. (1999) and Kuo et al. (2005) investigated the condensation HTC and frictional pressure drop of R134a and R410A in a vertical PHE. The experiments were carried out at mass fluxes range of 60 to 120 $kg\cdot m^{-2}\cdot s^{-1}$ for R134a and 50 to 150 $kg\cdot m^{-2}\cdot s^{-1}$ for R410A. The HTCs increase with mass flux indicating convective condensation. Grabenstein and Kabelac (2012) measured the condensation of R134a inside a PHE. Saturated vapor and saturated liquid were present at the inlet and outlet of the condenser respectively. Temperatures of the wall and the secondary fluid were measured at seven locations to obtain local HTCs. The mass flux range is 38-62 $kg\cdot m^{-2}\cdot s^{-1}$ and the HTCs increase with mass flux, indicating convective condensation.

Longo et al. (2015), Eq. (8), and Yan et al. (1999), Eq. (9), modified the correlation proposed by Akers et al. (1958) for condensation in horizontal tubes to extend the application to PHEs.

$$Nu_{cc} = \frac{\alpha_{cc}d_h}{\lambda_L} = 1.875\phi Re_{eq}^{0.445}Pr_L^{0.333} \quad (8)$$

$$Nu_{cc} = \frac{\alpha_{cc} d_h}{\lambda_L} = 4.118 Re_{eq}^{0.4} Pr_L^{0.333} \tag{9}$$

Recently Eldeeb et al. (2016) have published a more extensive review of correlations for the prediction of heat transfer and pressure drop during condensation in PHEs.

All reported research concludes that factors that enhance heat transfer also increase pressure drop. Independent of the condensation regime, pressure drop increases with mass flux and vapor quality. Yan et al. (1999) correlated the condensation pressure drop data as follows:

$$\Delta P = 2 f_{TP} \frac{G^2}{\rho_{av}} \frac{L_p}{d_h} \tag{10}$$

Where

$$\frac{1}{\rho_{av}} = \frac{(1-x)}{\rho_L} + \frac{x}{\rho_G} \tag{11}$$

and

$$f_{TP} = 94.75 Re_{eq}^{-0.0467} Re_{LO}^{-0.4} Bo^{0.5} \left(\frac{P}{P_{cr}} \right)^{0.8} \tag{12}$$

The liquid only Reynolds number, Re_{LO}, is defined by assuming all the fluid flow as liquid

$$Re_{LO} = \frac{G d_h}{\mu_L} \tag{13}$$

While the Boiling number, *Bo*, is defined as

$$Bo = \frac{\dot{q}}{G \Delta h_{LG}} \tag{14}$$

3.2 Temperature driving force, $\Delta T = T_{sat} - T_{wall}$ and heat flux, $\dot{q}$

The temperature difference between the wall and the refrigerant is directly related to the heat flux. A larger temperature difference contributes to larger heat flux. Generally, both temperature driving force and heat flux are the results of other operating conditions imposed on the system.

Mancin et al. (2012a) found that the HTCs of R407C and R410A decrease when the temperature difference increases. Also Jokar et al. (2004) studied the condensation of R134a and obtained that the effect of temperature driving force changes with the transition from film condensation to convective condensation. As temperature difference increases, HTCs

decrease sharply at gravity-controlled regime with small mass flux, and decrease slightly at convective regime.

Mancin et al. (2013) distinguished condensation regimes according to their dependence on temperature driving force. The dependent regime is gravity-controlled, while the independent regime corresponds to convective condensation. The HTC in the transition regime is a combination of both regimes. These three regimes are determined by the dimensionless gas velocity, j_G:

$$\begin{cases} j_G \le j_{G\_low}, & \text{temperature driving force dependent regime} \\ j_{G\_low} < j_G < j_{G\_high}, & \text{transition regime} \\ j_G \ge j_{G\_high}, & \text{temperature driving force independent regime} \end{cases} \tag{15}$$

where

$$j_G = \frac{xG}{\left[gd_h\rho_G(\rho_L-\rho_G)\right]^{0.5}} \tag{16}$$

and

$$j_{G\_low} = 0.89 - 0.93e^{-0.087\left[\left(\frac{1}{x}-1\right)^{0.8}\left(\frac{P}{P_{cr}}\right)^{0.4}\right]^{-1.17}} \tag{17}$$

$$j_{G\_high} = \left[\left(\frac{7.5}{4.3\left(\left(\frac{\mu_L}{\mu_G}\right)^{0.1}\left(\frac{\rho_G}{\rho_L}\right)^{0.5}\left(\frac{1-x}{x}\right)^{0.9}\right)^{1.11}+1}\right)^{-3} + 2.6^{-3}\right]^{-0.333} \tag{18}$$

Yan et al. (1999) and Kuo et al. (2005) investigated the effect of mean heat flux at constant mass flux and varying vapor qualities. HTCs increase with mean heat flux, but the effect is limited compared with mass flux.

In the experiments of Longo (2008, 2009, 2010a / b, 2011), the mean heat flux varies in accordance with the mass flux so that the vapor quality difference between the inlet and the outlet remains constant. Larger mass fluxes correspond to larger temperature driving forces. The experiments of Sarraf et al. (2015a) were performed in a similar way. The inlet and outlet conditions remain unchanged with the variation of mass fluxes. The analysis shows that the local heat flux is not constant. For certain large mass fluxes, the local heat flux varies by 400% along the condenser from the inlet to the outlet. Winkelmann (2010) changed the outlet vapor quality for the same mass flux. Higher outlet vapor quality is related to lower heat flux.

Yan et al. (1999) and Kuo et al. (2005) also analysed the influence on pressure drop, which increases slightly with mean heat flux. The conclusions of Djordjević et al. (2008) and Shi et al. (2010) are similar.

3.3 Vapor quality, *x*

Mancin et al. (2012a) demonstrated that the HTCs of R407C and R410A increase with outlet vapor quality when mass flux is maintained constant. The increase is specifically noticeable at larger mass fluxes. Eqs. (15) to (18) indicate vapor quality affects the transition from gravity-controlled condensation to convective condensation, which is shown in Fig. 4. The dimensionless gas velocity, j_G, is determined by mass flux and vapor quality, and is shown as a parameter. Transition dimensionless gas velocities, j_{G_low} and j_{G_high}, are determined by vapor quality alone and are also plotted as vertical lines in Fig. 4. The distinction of the condensation regimes is obtained by comparing the local values of j_G, j_{G_low} and j_{G_high} according to Eq. (15). At small mass flux, the condensation develops from gravity-controlled condensation to transition regime with decreasing vapor quality. The condensation is in the transition regime at larger mass flux independent of the vapor quality. Convective condensation does not appear in Fig. 4 because the mass flux is not large enough.

<figure 4>

Yan et al. (1999) and Kuo et al. (2005) reported that the HTCs increase with the vapor quality. The local R134a condensation experiments of Grabenstein and Kabelac (2012) showed that the local HTCs increase with mass flux at high vapor quality and stay nearly constant at lower vapor quality. Winkelmann (2010) reported a larger effect of vapor quality on HTCs for condensation of R134a compared to other researchers.

HTCs increase with vapor quality. This is expected because higher vapor qualities correspond to thinner condensate films and smaller heat transfer resistances. As indicated above, the results from several papers are consistent. Even though vapor quality decreases continuously along the flow direction of the refrigerant, the dependence on axial location is not exactly the same as vapor quality. In the inlet region the flow distribution is non-homogeneous and tends to become homogeneous after a certain length (Sarraf et al., 2015a, 2016).

3.4 Operating pressure, P

According to the experimental results of Longo (2008, 2009, 2010a / b, 2011), the operating pressure does not affect the transition mass flux and the values of the HTCs. Winkelmann (2010) also reported that the condensation pressure has no effect on the HTCs. However, Thonon and Bontemps (2002) found that the HTCs increase with condensation pressure in the gravity-controlled regime, and attributed this to the change of the refrigerant properties with pressure. Additionally, higher operating pressures lead to larger transition mass fluxes. Yan et al. (1999) and Kuo et al. (2005) obtained an opposite trend for the R134a and R410A condensation experiments: increasing condensation pressure results in slightly reduced HTCs. The main reasons are the reduction of the liquid thermal conductivity and the two-phase density ratio. The impact of operating pressure on the HTCs for R134a observed by Grabenstein and Kabelac (2012) is similar: higher condensation pressure reduces the HTCs at high vapor qualities but has no effect at low vapor qualities. This trend follows from Eqs. (8) and (9).

The influence of condensation pressure on pressure drop is not unanimous. The experiments of Longo (2010a / b), Yan et al. (1999) and Kuo et al. (2005) showed that the influence is small. Grabenstein and Kabelac (2012) proved that pressure drop decreases with increasing condensation pressure and the influence is more significant at larger mass flux. Winkelmann (2010), Wang and Zhao (1993) and Han et al. (2003) also confirmed that condensation pressure affects the pressure drop. The vapor density is larger at higher pressure and thus the vapor velocity is reduced. Higher reduced pressure and lower liquid dynamic viscosity lead to reduced pressure drop.

3.5 Inlet superheating, T_{sup}

The analysis of superheated vapor at the inlet of condensers is complex since it is difficult to determine the starting point of condensation. Hrnjak and Kondou (2013) proposed to consider that condensation starts where the wall temperature is below the saturation temperature.

Webb (1998) extended the application of Nusselt's (1916) equation, Eq. (7), to superheated vapor at the condenser inlet by adding the de-superheating specific enthalpy change to the latent heat of condensation. Longo (2008, 2009, 2011) also studied the effects of superheating. Superheating in the inlet does not affect the transition mass flux. The author assumed that superheated vapor condenses directly and there is no de-superheating region near the inlet that can be characterized as vapor single-phase heat transfer. Similarly, the

condensate film along the channel is subcooled and no subcooling region exists near the outlet operating as liquid single-phase heat transfer. The saturation temperature is used to calculate the logarithmic mean temperature difference and thereby to obtain the mean HTCs all over the channel. Superheating of vapor enhances HTCs compared with saturated condensation at the same mass flux. According to Longo, superheating affects condensation kinetics and reduces the condensate film thickness. Mancin et al. (2012a / b) assumed that the wall temperature is lower than the local dew temperature of the refrigerant at the inlet, so that superheated vapor condenses directly.

The infrared thermography experiments of Sarraf et al. (2016) indicated that the condensation region starts a distance from the inlet and ends apart from the outlet. The experiments demonstrate that PHE condensers actually have de-superheating and subcooling regions. The superheating zone has a positive effect on flow distribution and enhances the interfacial shear. Sarraf et al. (2016) confirmed that superheating does not affect the transition mass flux of condensation mechanisms, while the heat transfer enhancement is more significant at gravity-controlled regime than at convective regime. Moreover, they suggested the formation of condensation droplets at superheating zone, followed by droplets dragging and evaporation along the flow path by interfacial shear and gravity. Jokar et al. (2004, 2006) considered that there are de-superheating and subcooling regions, and predicted the areas of these regions by using single phase HTCs. The refrigerant was assumed to flow homogeneously.

Additionally, Sarraf et al. (2016) reported that the superheating increases pressure drop slightly at gravity-controlled regime and has a larger effect in the convective regime. On the other hand, Longo (2011) indicated the superheating exerts no effect on pressure drop.

3.6 Mixtures

Thonon and Bontemps (2002) identified a different behavior for mixtures: increasing mass flux contributes to higher HTCs in both condensation regimes. The heat transfer enhancement for small mass fluxes is even sharper. The mass transfer resistance associated with mixtures deteriorates the heat transfer. For small mass fluxes, the limited mixing in the gas phase increases the mass transfer resistance and reduces the HTC. For larger mass fluxes, mixing of the gas phase enhances mass transfer and increases the HTC. These authors used mixtures of butane and propane at different concentrations. Generally speaking, the HTC of mixtures is lower than that of both pure components, and is affected by the operating pressure.

3.7 Refrigerant properties

Condensation of refrigerants including HFCs, hydrocarbons and their mixtures in PHEs has been investigated by a large number of researchers. Longo (2010a / b) considered that, for pure refrigerants (R134a is most researched), the thermal conductivity of the liquid has the dominant effect among all the fluid properties. Moreover, Eqs. (6), (8) and (9) show that for higher vapor qualities the density ratio also plays a significant role. The performance of mixtures is much more complicated. However, according to Mancin et al. (2012a / b), zeotropic mixture R407C and near-azeotropic mixture R410A behave as pure fluids. Apart from the above fluids, R365mfc, R1234yf, R1234ze(E), R1234ze(Z) were investigated (Grabenstein and Kabelac, 2012; Longo and Zilio, 2013; Longo et al. 2014 a/ b). The research on the condensation of inorganic substances such as ammonia and carbon dioxide in PHEs is limited (Hayes et al. 2011; Hayes et al. 2012).

Wang and Zhao (1993) studied steam condensation heat transfer and pressure drop in a PHE. The results are different from the previously mentioned refrigerants: the Nusselt number increases with increasing mass flux but decreases with increasing vapor quality at the outlet. Heat transfer performance for complete condensation surpasses that of partial condensation. Increasing temperature differences reduces the Nusselt number.

In terms of pressure drop, Longo (2010a / b) concluded that R410A has the lowest pressure drop among R236fa, R134a and R410A at the same range of condensation temperature and mass flux, while the pressure drop of R1270 is lower than R600a and R290. Higher reduced pressure and lower liquid dynamic viscosity help to reduce pressure drop. Yan et al. (1999) and Kuo et al. (2005) compared R134a and R410A at different condensation temperatures and mass fluxes. The pressure drop of R410A is lower at high vapor quality but higher at low vapor quality.

3.8 Plate geometry

Han et al. (2003) measured the condensation HTC and the pressure drop in brazed PHEs with chevron angles of 45°, 55°, and 70°. R410A and R22 were tested with varying mass flux, condensation temperature, and vapor quality. The HTCs increase with mass flux and vapor quality, which indicates convective condensation. Larger chevron angles contribute to higher HTCs. The influence of chevron angles is more significant at large mass flux and high vapor quality. These authors proposed to modify the equation introduced by Yan et al. (1999), Eq.

(9), to consider the major geometric parameters, namely, the corrugation wave length, Λ_{wave}, the hydraulic diameter, d_h, and the chevron angle, β. Eq. (19) shows the modified equation.

$$Nu_{cc} = \frac{\alpha_{cc} d_h}{\lambda_L} = \left(11.22 \left(\frac{\Lambda_{wave}}{d_h} \right)^{-2.83} \beta^{-4.5} \right) Re_{eq}^{\left(0.35 \left(\frac{\Lambda_{wave}}{d_h} \right)^{0.23} \beta^{1.48} \right)} Pr_L^{0.333} \tag{19}$$

Table 1 compares the geometric parameters of several studies associated with Eqs. (8), (9) and (19). For instance, Han et al. (2003) tested the plate with a corrugation wavelength of 4.9 mm, a chevron angle of 70° (1.222 rad) and a hydraulic diameter of 3.68 mm, and thus Eq. (19) becomes Eq. (20). In Table 1, larger chevron angles are related to larger exponents of Re_{eq}, which suggests that HTCs are more sensitive to mass flux and vapor quality at larger chevron angles.

<Table 1>

$$Nu_{cc} = \frac{\alpha_{cc} d_h}{\lambda_L} = 2.026 Re_{eq}^{0.503} Pr_L^{0.333} \tag{20}$$

Mancin et al. (2012a) changed the number, length and width of plates in experiments. None of the tested PHEs shows evident superiority in terms of heat transfer, but less channels reduce maldistribution. Jin and Hrnjak (2017) showed that the end plates of PHEs function as fins and this effect can be significant when the plate number is small.

Amalfi et al. (2016b) conducted dimensional analysis for flow boiling in PHEs using least squares method and identified the chevron angles and the hydraulic diameters as the most important geometric parameters.

Han et al. (2003) reported that larger chevron angles lead to higher pressure drop, and proposed a two-phase fanning factor which takes the geometry into account:

$$f_{TP} = \left(3521.1 \left(\frac{\Lambda_{wave}}{d_h} \right)^{4.17} \beta^{-7.75} \right) Re_{eq}^{\left(-1.024 \left(\frac{\Lambda_{wave}}{d_h} \right)^{0.0925} \beta^{-1.3} \right)} \tag{21}$$

Eq. (21) becomes Eq. (22) with the same geometric parameters as in Eq. (20). When compared with Eq. (12), Eq. (22) shows more sensitivity to Re_{eq}, which is consistent with the conclusion by the authors that larger chevron angles intensify the effect of mass flux, vapor quality and condensation temperature on pressure drop.

$$f_{TP} = 2461.2 Re_{eq}^{-0.810} \quad (22)$$

Würfel and Ostrowski (2004) tested PHEs with neighbouring plates of 30°/30°, 30°/60° and 60°/60°. The pressure drop increases with chevron angles and the pressure drop of 30°/60° is between 30°/30° and 60°/60°.

4. Original studies on two-phase flow patterns

This section firstly describes flow patterns, and then summarizes the original visualization experiments used to obtain flow pattern data. Four main flow patterns, together with their transition regions, are chosen from all the flow phenomena to construct flow pattern maps. In order to develop combined maps, experimental conditions are given and assumptions are made for missing experimental details. These visualization experiments also measured pressure drop, which indicates two-phase flow characteristics. The original flow pattern maps using v_G versus v_L and x versus G are presented. This paper focuses on two-phase vertical downward flow in the overall channel between two PHE plates (Tribbe and Müller-Steinhagen, 2001b; Vlasogiannis et al., 2002; Nilpueng and Wongwises, 2010; Winkelmann, 2010; Grabenstein and Kabelac, 2012; Grabenstein et al., 2017). This corresponds to the preferred flow direction for condensers and absorbers.

4.1 Description of flow paths and flow patterns

Both flow paths and flow patterns are used to describe the two-phase flow characteristics. Flow paths are defined according to the flow direction in a channel, while flow patterns are mainly about the geometric configurations of gas and liquid, as well as the interface characteristic.

Representations of the two flow paths are given in Fig. 2. Depending on the PHE geometry, the flow path of the fluid inside the channel is either cross flow, also referred to as crossing flow, or wavy longitudinal flow. In the first case the flow path of the fluid is from one side of the plate to the other, and then it changes direction and moves along the adjacent plate. In the second case, the fluid changes direction at each crossing point of two adjacent plates.

Crossing flow is more observed in PHEs with small chevron angles to the main flow direction, while wavy longitudinal flow becomes observable with larger chevron angles. In many cases, both paths exist simultaneously. The central spine of the plate acts as a boundary to flow, directing approaching flow along the furrows of the adjacent plate. A detailed

description of flow paths is found in Stephan et al. (2010). Sarraf et al. (2015b) confirmed the coexistence of the two flow paths in their simulation of single-phase flow, and concluded that mass flux also has a distinct influence. Crossing flow is dominant at low mass flux. With the increase of mass flux, it is gradually converted into wavy longitudinal flow.

Flow patterns describe the two-phase flow distribution within a single channel. The flow patterns observed in PHEs are listed in Table 2. For the convenience of developing flow pattern maps in Sections 4 and 6, reference numbers are allocated to each study and are presented in the first column. All the studies described flow patterns similarly, but the transition position might change because of different chevron angles or working fluids, which are treated as specific characteristics (see third column). Grabenstein et al. (2017) tested two chevron angles but observed no significant effect on transitions, so chevron angles are not specific characteristics in this case. Detailed descriptions of the experimental conditions are given in Table 3. Four main flow patterns are considered in this study, and the other patterns are considered to be the transition between main flow patterns or the same as the main flow patterns but with different names. These four types are bubbly, slug, churn and film flow. This distinction is based on the described flow patterns in vertical tubes and PHEs. In addition, Table 2 presents the flow patterns in round mini tubes (Fukano and Kariyasaki, 1993; Mehta and Banerjee, 2014) for comparison purposes of flow pattern maps and will be discussed in section 6.3.

<Table 2>

Fig. 5 presents the four main flow patterns. The sequence is generally based on the occurrence of flow patterns when increasing the gas mass flux. For simplification, the channel walls are represented by straight lines rather than the actual geometry.

When the flow consists of a continuous liquid phase containing many bubbles smaller than the main channel dimensions, the flow is referred to as bubbly flow. This is the first main flow pattern and can be divided into regular and irregular bubbly flow. The bubbles are even sized with spherical shape for regular bubbly flow. With increasing gas mass flux, the flow transforms to irregular bubbly flow and the bubbles vary in size and shape.

Slug flow is the second main type and describes the flow of several large bubbles or slugs which are regularly shaped but have similar dimensions to the main channel. The slugs are formed from the coalescence of small bubbles and make the flow intermittent. The

characteristic shape of the slug resembles a bullet with a hemispherical nose and a blunt tail. Additionally, small bubbles may still be present for this flow pattern.

For churn flow, the two-phase flow becomes wavy and irregular, with the gas-phase still dispersed along the channels. Churn flow may include small bubbles in the liquid film apart from the gas bulk. In fact, it is difficult to quantitatively distinguish slug and churn flow. It is generally accepted that churn flow is the chaotic version of slug flow because the amount of liquid between the large bubbles is too little to form stable liquid zones. The liquid zones break up and contribute to the stir of the flow. In some cases, the fluid oscillates but retains a net velocity in the flow direction. Slug flow has smooth bubble boundaries and can be regarded as the transition between bubbly flow and churn flow.

Finally, film flow is sometimes treated as annular flow, since thin liquid film flows on the channel walls and continuous gas bulk flows in the middle. Rivulet or wavy flow are used when rivulets or waves appear on the film surface. Annular-liquid bridge flow occurs as the disturbances are strong enough to span from one side of the film to the other side, whose presence needs more liquid. The main difference between annular-liquid bridge and slug or churn is that the limited liquid bridge is not regarded as liquid zone that intermits the core of gas. As the amount of gas increases, the limited liquid film is unable to wet the entire surface so part of the surface dries up. The flow is then referred to as partial film flow.

Bubbly flow is a combination of large liquid mass flux and small gas mass flux, while film flow is composed of less liquid and more gas. When the mass fluxes of both phases are limited and no slug appears, the flow is regarded as transition between bubbly flow and film flow. The transition between flow patterns will be discussed in Section 6. It can be expected that flow patterns are associated with the condensation regimes previously introduced in Section 3.

<figure 5>

4.2 Operating conditions of visualization experiments

Generally, these studies used air-water under adiabatic conditions without phase changes. In the experiments of Nilpueng and Wongwises (2010), air-water were heated by hot water but without phase change. Grabenstein and Kabelac (2012) and Grabenstein et al. (2017) used R365mfc for both condensation and visualization experiments, but the visualization

experiments were adiabatic. Tribbe and Müller-Steinhagen (2001a) tested the pressure drop of air and aqueous solution of carboxymethylcellulose, but the visualization experiments were limited to air-water.

Table 3 summarizes the PHE geometries and the operating conditions used to develop combined flow pattern maps. The operating pressures were not all clearly reported. Only Vlasogiannis et al. (2002) reported clearly that the air flow was converted to atmospheric pressure. All experimental set-ups seem to have an atmospheric vessel in connection to the outlet of the PHE. When not reported, the operating pressure is taken as the atmospheric pressure added with 50% of the reported pressure drop. Furthermore, the authors have compared different operating temperatures and pressures, whose effects on fluid properties is limited. The geometries of the PHEs were different in all the studies, and were not clearly reported for certain cases. Table 3 presents the geometric details and the distributors.

<Table 3>

4.3 Pressure drop without phase change

Nilpueng and Wongwises (2010) carried out experiments on both upward and downward flow. The plate tested is unsymmetrical. The results of both flow directions are similar. Pressure drop is enlarged by two-phase velocities. In the downward experiment of Grabenstein and Kabelac (2012), pressure drop increases with liquid velocity continuously. But with growing vapor velocity, pressure drop increases at first and decreases at higher value. This may be related to the change of flow pattern. Winkelmann (2010) studied adiabatic two-phase flow in downward direction. Higher mass flux and vapor quality contribute to larger pressure drop.

Tribbe and Müller-Steinhagen (2001a) measured the pressure drop in a single channel of PHEs with different chevron angles, channel gaps and flow directions. Air-water and air-carboxymethylcellulose solution were used as the working fluids. Similar to the above researches, mass flux, vapor quality and two-phase velocities have a positive and monotonous effect on pressure drop. The pressure drops of inlet and outlet sections were excluded when analysing the effect of chevron angles. Pressure drop of the corrugated section increases with chevron angle. Pressure drop of mixed chevron angles is between that of larger and smaller angles. Flow directions have negligible effects on pressure drop below 400 $kg \cdot m^{-2} \cdot s^{-1}$, which

is the mass flux range of most PHEs. Pressure drop of upward flow is distinctly higher than downward flow at higher mass fluxes. The viscosity of carboxymethylcellulose solution is much higher than water. At low vapor quality, viscous solution undergoes higher pressure drop. The deviation diminishes with rising vapor quality.

4.4 Presentation of original flow pattern maps

Winkelmann (2010) presented no separating lines between flow patterns, which are assumed to be straight lines in the original map. Other studies included separating lines.

Except for Grabenstein et al. (2017), all the studies presented the maps in the form of two-phase superficial velocities (v_G versus v_L), which are combined in Fig. 6. Fluid properties and geometries are not incorporated into axes parameters. Dimensionless quantities are preferred to consider these parameters.

<figure 6>

Section 3 indicates that mass flux and vapor quality play important roles in condensation, which are used to present separating lines in Fig. 7. The square root of vapor quality is used to expand the regions of flow patterns at low vapor quality and improve the readability.

<figure 7>

Visualization experiments on PHEs have been conducted for different flow directions and plate geometries. Nilpueng and Wongwises (2010) also investigated vertical upward flow, the flow patterns of which are different from downward flow. Jassim et al. (2001, 2006) focused on the upward flow in both chevron and bumpy style PHEs. Asano et al. (2004a / b, 2005) studied the void fraction distribution of two-phase flow in a PHE making use of neutron radiography. Vakili-Farahani et al. (2014a / b) obtained the pressure profile of upward two-phase flow for both adiabatic and boiling conditions using infrared thermography. Gradeck and Lebouche (2000) discussed horizontal flow patterns in PHEs. Shiomi et al. (2004) investigated the flow patterns of both horizontal and upward flow in PHEs with different chevron angles.

5. Relevant parameters in flow pattern determination

Flow patterns are mainly affected by the geometric characteristics, interaction of forces, fluid properties and two-phase velocities. Geometric parameters are discussed in Section 2. The other parameters are presented and made non-dimensional in this section.

5.1 Non-dimensional parameters for forces in two-phase flow

The Reynolds number is the ratio of inertia to viscous forces. Heat transfer and pressure drop studies have proposed the equivalent Reynolds number for two-phase flow, Re_{eq}, Eq. (6), which is relevant for homogeneous two-phase flow, such as bubbly flow. The liquid Reynolds number, Re_{L}, is defined by just considering the mass flux of liquid phase (Longo, 2008):

$$Re_L = \frac{G(1-x)d_h}{\mu_L} \tag{23}$$

The Froude number is the ratio of inertia to gravity and is expected to play a role in vertical PHEs. The Froude number for vertical two-phase flow is given by Oshinowo and Charles (1974) and Bergles et al. (1981):

$$Fr_{TP,ver} = \frac{(v_G + v_L)^2}{gd_h} \tag{24}$$

Stephan et al. (2010) used the dimensionless gas velocity, j_G, defined by Eq. (16), as the Froude number for horizontal two-phase flow. Its application in vertical two-phase flow will be investigated in Section 6.2.

$$Fr_{TP,hor} = j_G = \frac{xG}{\left[gd_h\rho_G(\rho_L - \rho_G)\right]^{0.5}} \tag{25}$$

The Weber number is the ratio of inertia to surface tension and might play a role for flow patterns, which is given by Stephan et al. (2010):

$$We = \frac{\rho v^2 d_h}{\sigma} \tag{26}$$

Finally, the Bond number is the ratio of gravity to surface tension, and is expected to be non-negligible at low mass flux (Bergman et al., 2011):

$$Bd = \frac{(\rho_L - \rho_G) g d_h^2}{\sigma} \tag{27}$$

In the analysis of flow patterns, these parameters should be clearly distinguished such as Froude numbers for both vertical and horizontal two-phase flow, equivalent Reynolds number and liquid Reynolds number.

5.2 Non-dimensional parameters for fluid properties and velocities

For two-phase flow in tubes, different dimensionless quantities are used to predict the flow patterns. Hewitt and Roberts (1969) predicted flow patterns in horizontal tubes and presented a flow pattern map, but the quantities in the axes are not dimensionless. Oshinowo and Charles (1974) proposed flow pattern maps for both upward and downward flow in tubes with dimensionless quantities. The Froude number is used in the x-axis as given by Eq. (24). A property modifying parameter, Λ, is defined as a function of the liquid properties relative to those of water under the same conditions (Oshinowo and Charles, 1974):

$$\Lambda = \frac{\mu_L / \mu_W}{\left[\frac{\rho_L}{\rho_W} \left(\frac{\sigma_L}{\sigma_W} \right)^3 \right]^{1/4}} \tag{28}$$

The two dimensionless quantities are combined in the x-axis as $Fr_{TP,\mathrm{ver}} / \Lambda^{0.5}$. The y-axis presents the square root of the delivered gas to liquid volume ratio, R_v, which is given as the ratio of gas and liquid superficial velocities (Oshinowo and Charles, 1974):

$$R_v = \frac{\dot{V}_G}{\dot{V}_L} = \frac{v_G}{v_L} \tag{29}$$

The superficial gas and liquid velocities, v_G and v_L, are obtained from:

$$v_G = \frac{\dot{V}_G}{W_p d_g} \tag{30}$$

$$v_L = \frac{\dot{V}_L}{W_p d_g} \tag{31}$$

Dobson and Chato (1998) studied condensation in horizontal smooth tubes and presented a flow pattern map in mass flux - vapor quality (*G*-*x*) axes as shown in Fig. 7. These parameters have been widely adopted in tube studies.

6. Construction of combined flow pattern maps

Efforts are made in this section to translate the original flow pattern maps for two-phase downward flow in PHEs to new maps. Apart from *G-x*, a series of axes combinations have been evaluated. Grabenstein et al. (2017) presented flow pattern maps using $\rho_G v_G^2$ versus $\rho_L v_L^2$. Spedding et al. (1998) also compared $\rho_G v_G^2$ versus $\rho_L v_L^2$, and additionally $\left(We_G Re_G \left[R_v/(R_v+1)\right]\right)^{0.5}$ versus $\left(We_L Re_L \left[1/(R_v+1)\right]\right)^{0.5}$. In the present analysis, the separating lines diverge in the map of the first combination, while the separating lines overlap at low values of $\left(We_G Re_G \left[R_v/(R_v+1)\right]\right)^{0.5}$ in the map of the second combination. Also in the map of $Re_{eq}/\Lambda^{0.5}$ versus $R_v^{0.5}$, the separating lines deviate from each other. Among all the investigated combinations, $Fr_{TP,ver}/\Lambda^{0.5}$ versus $R_v^{0.5}$ and Re_L versus $Fr_{TP,hor}/\Lambda^{0.5}$ show better performance, and will be introduced in the following sub-sections.

6.1 Flow pattern map based on $Fr_{TP,ver}/\Lambda^{0.5}$ versus $Rv^{0.5}$

$Fr_{TP,ver}/\Lambda^{0.5}$ versus $R_v^{0.5}$ was proposed by Oshinowo and Charles (1974). These parameters include superficial velocities, PHE geometries and fluid properties. Most of the fluid properties are computed using Refprop (Lemmon et al., 2013), while the surface tension values between air-water are taken from Vargaftik et al. (1983).

Fig. 8 plots all the separating lines between flow patterns. The zones of the flow patterns are indicated by the marks. The y-axis is limited to $R_v^{0.5} \leq 20$ to improve the readability. Thus some of the separating lines from Winkelmann (2010) are left out.

<figure 8>

Fig. 9 presents a simplified flow pattern map based on Fig. 8, which takes into account the most important flow patterns. The flow is film/partial film at large volume ratio of gas to liquid. At small ratio, the flow changes from regular bubbly, irregular bubbly to slug flow with increasing Froude numbers. Transition between bubbly and film flow appears at small

Froude numbers, while churn flow appears between slug and film/partial film flow at large Froude numbers. The film/partial film flow also includes the annular, annular-liquid bridge (unstable), wavy and rivulet (partially wetting) flow. Unfortunately, this combination of dimensionless parameters does not eliminate the overlap of different flow patterns.

<figure 9>

6.2 Flow pattern map based on Re_L versus $Fr_{TP,hor}/\Lambda^{0.5}$

Fig. 10 is a flow pattern map making use of the dimensionless parameters Re_L versus $Fr_{TP,hor} / \Lambda^{0.5}$ as defined in Section 5, which account for inertia, viscous force and gravity. Re_L includes the dimensionless liquid phase mass flux, while $Fr_{TP,hor} / \Lambda^{0.5}$ includes the dimensionless gas phase mass flux. This combination takes also mass flux and vapor quality into account. The map is presented in simplified form in Fig. 11 to include only the most relevant information. Dashed lines instead of solid lines are used between similar flow patterns. Film flow is encountered at small liquid mass flux even if the gas mass flux is small. At larger liquid mass fluxes, the flow becomes regular bubbly, irregular bubbly, slug, churn and film flow with increasing gas mass flux. Additionally, transition between bubbly flow and film flow takes place at intermediate liquid mass flux. There is partial film flow at small liquid mass flux and large gas mass flux.

<figure 10>

<figure 11>

Constant vapor quality lines can be constructed in the map. Eq. (32) is the ratio of both axes and depends on vapor quality:

$$\frac{Fr_{TP,hor} / \Lambda^{0.5}}{Re_L} = \frac{G_G}{\left[g d_h \rho_G (\rho_L - \rho_G) \right]^{0.5} \Lambda^{0.5}} \frac{\mu_L}{G_L d_h} = \delta \frac{G_G}{G_L} = \delta \frac{x}{1-x} \tag{32}$$

where

$$\delta = \frac{\mu_L}{\left[gd_h\rho_G(\rho_L-\rho_G)\right]^{0.5}\Lambda^{0.5}d_h} \tag{33}$$

and

$$x = \frac{G_G}{G_L+G_G} \tag{34}$$

Constant overall mass flux lines can be constructed by adding both axes as illustrated in Eqs. (35) and (36):

$$\frac{Fr_{TP,hor}}{\Lambda^{0.5}} + Re_L = \frac{G_G}{\left[gd_h\rho_G(\rho_L-\rho_G)\right]^{0.5}\Lambda^{0.5}} + \frac{G_L d_h}{\mu_L} = \frac{1}{\zeta}\left[G_G + G_L + \left(\zeta\frac{d_h}{\mu_L}-1\right)G_L\right] \tag{35}$$

$$\frac{Fr_{TP,hor}}{\Lambda^{0.5}} = \frac{1}{\zeta}\left[G + \left(\zeta\frac{d_h}{\mu_L}-1\right)\frac{\mu_L}{d_h}Re_L\right] - Re_L = \frac{G}{\zeta} - \frac{\mu_L}{\zeta d_h}Re_L \tag{36}$$

where

$$\zeta = \left[gd_h\rho_G(\rho_L-\rho_G)\right]^{0.5}\Lambda^{0.5} \tag{37}$$

and

$$G = G_L + G_G \tag{38}$$

The condensation process can be depicted in the flow pattern map by considering a constant overall mass flux line with decreasing vapor quality. In Fig. 12, the experiment with R601 from Sarraf et al. (2015a) is taken as an example. At small mass flux such as 9 kg·m^{-2}·s^{-1}, the condensation takes place in film flow. At larger mass flux such as 29.8 kg·m^{-2}·s^{-1}, the condensation starts in film flow, changes from churn to slug, and ends up in transition flow. Sarraf et al. (2015a) concluded that the condensation is gravity-controlled when the mass flow is smaller than 15 kg·m^{-2}·s^{-1}, and convection-controlled at larger mass fluxes. Gravity-controlled condensation corresponds to film flow in the flow pattern map. Convection-controlled condensation is more complex since several flow patterns are involved.

<figure 12>

A comparison can be made with Fig. 4: film flow agrees qualitatively with the gravity-controlled condensation in the region of small mass flux and high vapor quality. The transition regime is equivalent to a series of flow patterns started from film flow in the map.

It needs to be noted that Fig. 11 is mainly based on air-water experiments while two-phase refrigerants are used for comparison. The fluid properties are compared in Table 4 and vary significantly. A deep understanding on the influence of fluid properties is needed before a quantitative comparison between flow patterns and condensation regimes can be made.

<Table 4>

6.3 Comparison with flow pattern maps of tubes

In order to validate the present flow pattern map, a comparison is made with round mini tubes whose diameters are comparative with the hydraulic diameters of PHEs. It is expected that flow patterns are affected by geometric structure, flow direction and working fluid (Fukano and Kariyasaki, 1993; Mehta and Banerjee, 2014; Chen et al. 2006). So the maps based on the downward flow of air-water within mini tubes have been selected for comparison purposes. Table 2 lists the reported flow patterns. Fukano and Kariyasaki (1993) did not distinguish elongated bubbly, slug and churn, stating these patterns as intermittent flow (Barnea et al. 1983). Mehta and Banerjee (2014) introduced the transition patterns of slug-bubbly and slug-annular.

Fig. 13 presents the comparison. According to Fukano and Kariyasaki (1993), the flow is annular at small liquid mass flux and large gas mass flux. It becomes dispersed bubbly with more liquid and less gas. Annular flow and dispersed bubbly flow are separated by a large region of intermittent flow.

<figure 13>

In Fig. 13, the separating lines from Mehta and Banerjee (2014) are vertical and horizontal, which indicates that the transition happens at constant mass fluxes of liquid or gas. The flow is annular at small liquid mass flux. Slug appears at intermediate two-phase mass fluxes, and changes to churn with increasing liquid and gas. Bubbly flow occurs at large amount of liquid and small amount of gas. Slug-bubbly and slug-annular are introduced to account for the gradual transition of flow patterns.

In general, the present flow pattern map is consistent with the maps of tubes regarding the position of patterns and transition trends. It is film flow when gas phase is dominant, while bubbly flow appears when liquid is the major phase. When both phases are of equivalent amount, the flow is slug or churn. Churn is the chaotic version of slug. Nevertheless, the separating lines show poor agreement. This is partly attributed to the determination of flow patterns. For instance, Fukano and Kariyasaki (1993) classified elongated bubbly as intermittent flow, which is similar to irregular bubbly in the present map. Moreover, the separating lines show a general shift. In the map of PHEs, the bubbly flow occupies a larger region. Corrugation structure may contribute to the breakup of gas volume and make it difficult for the bubbles to coalesce. For PHEs, the separating line of film shifts to the left, which corresponds to smaller liquid mass flux. Film is transformed into slug or churn when the waves on the film surface are large enough to connect to the film on the other side and intermit the gas. Thus certain amount of liquid is required. The corrugation of PHEs is likely to promote the development of waves and make the transition happen with less liquid. PHEs enhance the stir and mix of two-phase flow, therefore validation is necessary before referring to the maps of other geometries.

6.4 Deviation in the construction of the flow pattern maps

More reliable data are needed to improve the combined flow pattern maps and carry out quantitative analysis. Several causes are identified to explain the deviation of separating lines or the overlap of different flow patterns:

Subjectivity of observations in flow pattern determination: the subjectivity of observations affects the determination of flow patterns and their transitions in three ways. First of all, the flow patterns in PHEs are not clearly defined and the description is not consistent. The judgement of flow patterns depends on researchers. For example, some researchers neglect the distinction between regular bubbly and irregular bubbly flow. Additionally, the film and annular flow are similarly described and can be treated as the same. Secondly, the separating lines between flow patterns are determined subjectively. Flow patterns are observed for discrete operating conditions. When two neighboring data points represent different flow patterns, a separating line is usually constructed without strong evidence. As stated before, Winkelmann (2010) did not provide the separating lines, which

are constructed in this paper. Finally, the imaging conditions may influence the perception of the observers, including the lighting, the produced images and the type of transparent plate.

Different structure of distributor: the distributors of PHEs have a direct influence on the two-phase distribution at the inlet and further affect the flow patterns in the channel. Different structures were used in the visualization experiments, which are listed in Table 3.

Incomplete reporting of experimental conditions: certain geometric parameters of the plate are not clearly defined, such as the wavelength, Λ_{wave}, which is adopted to construct the flow pattern maps. The pressure, *P*, and temperature, *T,* are not reported in every study. In this case, a common pressure of 1 bar plus half of the pressure drop and room temperature (25 °C) are assumed, which affects the fluid properties. Additionally, the surface tension of air-water is calculated from a simplified table only based on temperature (Vargaftik et al., 1983).

Experimental uncertainties and plotting deviations: Experimental uncertainties include measurement accuracies of the pressure, the temperature and the two-phase superficial velocities, as well as random errors in the experiment. Not all authors report sufficiently on these uncertainties. In addition, the data are converted from original flow pattern maps to combined maps, whose accuracy is inferior to data sets.

7. Future work

In order to improve the accuracy of combined flow pattern maps, the deviations discussed in Section 6.4 should be minimized by complete reports of geometric parameters and operating conditions, and uncertainty analysis of experiments. Subjectivity of observations can only be reduced by setting up a recognized program for visualization experiment. Ideally, the experiments are performed by one research group or even one researcher. Or at least the researchers are suggested to report their work clearly and in a detailed way, as well as provide the original visualization pictures so that their determination can be confirmed. The program includes several requirements:

- Clear and consistent definitions and descriptions of flow patterns.
- Generally accepted flow pattern images that can be used as a reference.
- The transition between flow patterns. Visualization of two-phase flow in tubes shows that flow patterns change gradually with two-phase mass flux (Bhagwat and Ghajar, 2012).

Identifiable characteristics should be used as a reference to place separating lines. It is suggested that more measurement points are collected in the transition region between flow patterns.

- Unified criteria for lighting conditions, imaging quality and the thickness and material of transparent plates.

To gain insight in the factors determining flow patterns, both theoretical and experimental work is needed. Given the fact that flow mechanisms within PHEs are complex and limited theoretical results have been achieved, the theory applicable for round tubes or other geometries can be taken as a departing point. This paper proposes a dimensionless flow pattern map originally developed for round tubes (Oshinowo and Charles, 1974), but also a map with the dimensionless liquid and gas mass fluxes. The second flow pattern map seems to be more applicable than the original maps, and also indicates overall mass flux and vapor quality. A comparison is made with the map of round mini tubes, which indicates the influence of PHEs structure. Experiments need to be conducted under varying operating conditions (temperatures, pressures and inlet conditions), of different working fluids (such as refrigerants) and making use of different PHE geometries. The detailed geometric parameters have direct effects on flow patterns, and the overall geometric parameters play roles when PHEs are expanded to large scales.

Flow pattern maps help to deepen the understanding of condensation mechanisms. In order to compare flow patterns with condensation regimes quantitatively, more local measurements of condensation are needed including local vapor qualities and local heat transfer performance. It is suggested that flow patterns and local measurements of condensation are achieved within the same geometric structures and with the same working fluid. The focus may be on adiabatic flow in the first case, and later be expanded to flow with phase change.

It will be helpful to construct a universal flow pattern map, which is valid for different working fluids, operating conditions and PHE geometries. Given the dramatic difference of fluid properties, it seems difficult to integrate all the fluids in a single map. El Hajal et al. (2003) proposed universal flow pattern maps for horizontal tubes using G versus x, which apply to different fluids. The general positions of flow patterns are determined in the maps, but the separating lines depend on fluid properties and are calculated by equations. It is expected to build a flow pattern map of PHEs for a certain kind of fluid, and then to expand the map to other fluids by modifying the separating lines. In order to develop equations of

separating lines, a validated void fraction model is needed, which goes beyond the scope of this paper.

8. Conclusions

This work considers the two-phase downward flow within PHEs and covers condensation mechanisms and flow patterns. The major results can be summarized below:

- The transition from gravity-controlled condensation to convective condensation is mainly affected by mass flux and vapor quality. Other factors also have an influence on heat transfer and pressure drop.
- Two combined flow pattern maps are constructed making use of $Fr_{TP,\mathrm{ver}} / \Lambda^{0.5}$ versus $R_v^{0.5}$ and Re_L versus $Fr_{TP,hor} / \Lambda^{0.5}$. The second map predicts the transition of flow patterns well, and agrees qualitatively with the model of condensation mechanisms which considers overall mass flux and vapor quality. Furthermore, this map is compared with maps for downward two-phase flow in mini-tubes, indicating that maps for tubes cannot be directly applied to PHEs.
- Recommendations are given to optimize the combined flow pattern maps and to use the maps for the quantitative prediction of condensation mechanisms. Better predictions of the flow patterns in PHEs will improve the calculation of heat transfer and pressure drop.

Acknowledgements

This project has been developed in cooperation with Bluerise BV. X.T. and C.A.I.F. would like to acknowledge the financial support from the China Scholarship Council and from the Koude Groep Delft / Wageningen.

References

Abu-Khader, M. M., 2012. Plate heat exchangers: Recent advances. Renew. Sust. Energ. Rev. 16, 1883-1891.

Akers, W. W., Deans, H. A., Crosser, O. K., 1958. Condensing heat transfer within horizontal tubes. Chem. Eng. Progr. 54, 89-90.

Amalfi, R.L., Vakili-Farahani, F., Thome, J.R., 2016a. Flow boiling and frictional pressure gradients in plate heat exchangers. Part 1: Review and experimental database. Int. J. Refrig. 61, 166-184.

Amalfi, R.L., Vakili-Farahani, F., Thome, J.R., 2016b. Flow boiling and frictional pressure gradients in plate heat exchangers. Part 2: Comparison of literature methods to database and new prediction methods. Int. J. Refrig. 61, 185-203.

Asano, H., Takenaka, N., Fujii, T., Maeda, N., 2004a. Visualization and void fraction measurement of gas-liquid two-phase flow in plate heat exchanger. Appl. Radiat. Isot. 61, 707-713.

Asano, H., Takenaka, N., Fujii, T., 2004b. Flow characteristics of gas-liquid two-phase flow in plate heat exchanger (Visualization and void fraction measurement by neutron radiography). Exp. Therm. Fluid Sci. 28, 223-230.

Asano, H., Takenaka, N., Wakabayashi, T., 2005. Visualization and void fraction distribution of downward gas liquid two-phase flow in a plate heat exchanger by neutron radiography. Nucl Instrum Methods Phys Res A. 542, 154-160.

Barnea, D., Luninski, Y., Taitel, Y. 1983. Flow pattern in horizontal and vertical two phase flow in small diameter pipes. Can. J. Chem. Eng. 61, 617-620.

Bergles, A. E., Collier, J. G., Delhaye, J M., Hewitt, G. F., Mayinger, F., 1981. Two-phase flow and heat transfer in the power and process industries. Hemisphere, New York.

Bergman, T., Incropera, F., DeWitt, D., Lavine, A., 2011. Fundamentals of heat and mass transfer. John Wiley & Sons, 7th Edition, United States.

Bhagwat, S.M., Ghajar, A.J., 2012. Similarities and differences in the flow patterns and void fraction in vertical upward and downward two phase flow. Exp. Therm. Fluid Sci. 39, 213-227.

Chen, L., Tian, Y. S., Karayiannis, T. G., 2006. The effect of tube diameter on vertical two-phase flow regimes in small tubes. Int. J. Heat Mass Transf. 49, 4220-4230.

Dobson, M. K., Chato, J. C., 1998. Condensation in Smooth Horizontal Tubes. ASME J. Heat Transfer 120, 193-213.

Dović, D., Palm, B., Svaić, S., 2009. Generalized correlations for predicting heat transfer and pressure drop in plate heat exchanger channels of arbitrary geometry. Int. J. Heat Mass Transf. 52, 4553-4563.

Djordjević, E. M., Kabelac, S., Šerbanović, P. S., 2008. Heat transfer coefficient and pressure drop during refrigerant R-134a condensation in a plate heat exchanger. Chem Pap. 62, 78-85.

Eldeeb, R., Aute, V., Radermacher, R., 2016. A survey of correlations for heat transfer and pressure drop for evaporation and condensation in plate heat exchangers. Int. J. Refrig. 65, 12-26.

El Hajal, J., Thome, J.R., Cavallini, A., 2003. Condensation in horizontal tubes, part 1: two-phase flow pattern map. Int. J. Heat Mass Transf. 46, 3349-3363.

Freund, S., Kabelac, S., 2010. Investigation of local HTCs in plate heat exchangers with temperature oscillation IR thermography and CFD. Int. J. Heat Mass Transf. 53, 3764-3781.

Fukano, T., Kariyasaki A., 1993. Characteristics of gas-liquid two-phase flow in a capillary tube. Nucl. Eng. Des. 141, 59-68.

Grabenstein, V., Kabelac, S., 2012. Experimental and theoretical analysis of the local condensation heat transfer in a plate heat exchanger. J Phys Conf Ser. 395, 012169.

Grabenstein, V., Polzin, A.-E., Kabelac, S., 2017. Experimental investigation of the flow pattern, pressure drop and void fraction of two-phase flow in the corrugated gap of a plate heat exchanger. Int. J. Multiph. Flow. 91, 155-169.

Gradeck, M. Lebouche, M., 2000. Two-phase gas-liquid flow in horizontal corrugated channels. Int. J. Multiph. Flow. 26, 435-443.

Han, D.-H., Lee, K.-J., Kim, Y.-H., 2003. The characteristics of condensation in brazed plate heat exchangers with different chevron angles. Journal of the Korean Physical Society 43, 66-73.

Hayes, N., Jokar, A., Ayub, Z. H., 2011. Study of carbon dioxide condensation in chevron plate exchangers; heat transfer analysis. Int. J. Heat Mass Transf. 54, 1121-1131.

Hayes, N., Jokar, A., Ayub, Z. H., 2012. Study of carbon dioxide condensation in chevron plate exchangers; pressure drop analysis. Int. J. Heat Mass Transf. 55, 2916-2925.

Hewitt, V, Roberts, D. N., 1969. Studies of two-phase flow patterns by simultaneous X-ray and flash photography. Tech. rep., United Kingdom Atomic Energy Authority, Harwell.

Hrnjak, P., Kondou, C., 2013. Refrigerant side heat transfer in condensers with round tubes. Proceedings of the 4th IIR Conference on Thermophysical Properties and Transfer Processes of Refrigerants, Delft, The Netherlands, paper TP-087.

Hu, H., Zhang, R., Zhuang, D., Ding, G., Wei, W., 2015. Numerical model of two-phase refrigerant flow distribution in a plate evaporator with distributors. Appl. Therm. Eng. 75, 167-176.

Jassim, E. W., Newell, T. A., Chato, J. C., 2001. Investigation of adiabatic refrigerant pressure drop and flow visualization in flat plate evaporators. Technical report TR-187, Air Conditioning and Refrigeration Center, University of Illinois, Urbana-Champaign.

Jassim, E. W., Newell, T. A., Chato, J. C., 2006. Two-Phase flow visualization in chevron and bumpy style flat plate heat exchangers. Heat Transf. Eng. 27, 20-27.

Jin, S., Hrnjak, P., 2017. Effect of end plates on heat transfer of plate heat exchanger. Int. J. Heat Mass Transf. 108, 740-748.

Jokar, A., Eckels, S.J., Hosni, M.H., Gielda, T.P., 2004. Condensation heat transfer and pressure drop of the brazed plate heat exchangers using R-134a. Journal of Enhanced Heat Transfer 11, 161–182.

Jokar, A., Hosni, M.H., Eckels, S.J., 2006. Dimensional analysis on the evaporation and condensation of refrigerant R-134a in minichannel plate heat exchangers. Appl. Therm. Eng. 26, 2287-2300.

Jung, C. W., An, S. S., Kang, Y. T., 2014. Thermal performance estimation of ammonia-water plate bubble absorbers for compression/absorption hybrid heat pump application. Energy. 75, 371-378.

Kuo, W. S., Lie, Y. M., Hsieh, Y. Y., Lin, T. F., 2005. Condensation heat transfer and pressure drop of refrigerant R-410A flow in a vertical plate heat exchanger. Int. J. Heat Mass Transf 48(25): 5205-5220.

Le Lostec, B., Galanis, N., Millette, J., 2013. Simulation of an ammonia-water absorption chiller. Renew. Energy. 60, 269-283.

Lemmon, E. W., Huber, M. L., and McLinden, M. O. (2013). NIST Standard Reference Database 23: Reference Fluid Thermodynamic and Transport Properties-REFPROP, Version 9.1, National Institute of Standards and Technology, Standard Reference Data Program, Gaithersburg.

Longo, G.A., 2008. Refrigerant R134a condensation heat transfer and pressure drop inside a small brazed plate heat exchanger. Int. J. Refrig. 31, 780-789.

Longo, G.A., 2009. R410A condensation inside a commercial brazed plate heat exchanger. Exp. Therm. Fluid Sci. 33, 284-291.

Longo, G.A., 2010a. Heat transfer and pressure drop during HFC refrigerant saturated vapour condensation inside a brazed plate heat exchanger. Int. J. Heat Mass Transf. 53, 1079-1087.

Longo, G.A., 2010b. Heat transfer and pressure drop during hydrocarbon refrigerant condensation inside a brazed plate heat exchanger. Int. J. Refrig. 33, 944-953.

Longo, G.A., 2011. The effect of vapour super-heating on hydrocarbon refrigerant condensation inside a brazed plate heat exchanger. Exp. Therm. Fluid Sci. 35, 978-985.

Longo, G.A., Zilio, C., 2013. Condensation of the low GWP refrigerant HFC1234yf inside a brazed plate heat exchanger. Int. J. Refrig. 36(2): 612-621.

Longo, G.A., Zilio, C., Righetti, G., Brown, J.S., 2014a. Condensation of the low GWP refrigerant HFO1234ze(E) inside a Brazed Plate Heat Exchanger. Int. J. Refrig. 38, 250-259.

Longo, G.A., Zilio, C., Righetti, G., Brown, J.S., 2014b. Experimental assessment of the low GWP refrigerant HFO-1234ze (Z) for high temperature heat pumps. Exp. Therm. Fluid Sci 57: 293-300.

Longo, G.A., Righetti, G., Zilio, C., 2015. A new computational procedure for refrigerant condensation inside herringbone-type Brazed Plate Heat Exchanger. Int. J. Heat Mass Transf. 82, 530-536.

Mancin, S., Del Col, D., Rossetto, L., 2012a. Partial condensation of R407C and R410A refrigerants inside a plate heat exchanger. Exp. Therm. Fluid Sci. 36, 149-157.

Mancin, S., Del Col, D., Rossetto, L., 2012b. Condensation of superheated vapour of R410A and R407C inside plate heat exchangers: Experimental results and simulation procedure. Int. J. Refrig. 35, 2003-2013.

Mancin, S., Del Col, D., Rossetto, L., 2013. R32 partial condensation inside a brazed plate heat exchanger. Int. J. Refrig. 36, 601-611.

Mehta, H. B., Banerjee J., 2014. An investigation of flow orientation on air–water two-phase flow in circular minichannel. Heat Mass Transfer. 50, 1353-1364.

Metwally, H. M., Manglik, R. M., 2004. Enhanced heat transfer due to curvature-induced lateral vortices in laminar flows in sinusoidal corrugated-plate channels. Int. J. Heat Mass Transf. 47, 2283-2292.

Muley, A., Manglik, R. M., 1999. Experimental study of turbulent flow heat transfer and pressure drop in a plate heat exchanger with chevron plates. ASME J. Heat Transfer. 121, 110-117.

Nilpueng, K., Wongwises, S., 2010. Two-phase gas-liquid flow characteristics inside a plate heat exchanger. Exp. Therm. Fluid Sci. 34, 1217-1229.

Nusselt, W., 1916. Die Oberflachenkondensation des Wasserdampfes. Z. Ver. D. Ing. 60, 541-546.

Oshinowo, T., Charles, M. E., 1974. Vertical Two-Phase Flow. I Flow pattern correlations. Can. J. Chem. Eng. 52, 25-35.

Sarraf, K., Launay, S., El Achkar, G., Tadrist, L., 2015a. Local vs global heat transfer and flow analysis of hydrocarbon complete condensation in plate heat exchanger based on infrared thermography. Int. J. Heat Mass Transf. 90, 878-893.

Sarraf, K., Launay, S., Tadrist, L., 2015b. Complex 3D-flow analysis and corrugation angle effect in plate heat exchangers. Int. J. Therm Sci. 94, 126-138.

Sarraf, K., Launay, S., Tadrist, L., 2016. Analysis of enhanced vapor desuperheating during condensation inside a plate heat exchanger. Int. J. Therm Sci. 105, 96-108.

Shi, Z. Y., Chen, J. P., Grabenstein, V., Kabelac, S., 2010. Experimental investigation on condensation heat transfer and pressure drop of R134a in a plate heat exchanger. Heat mass transfer 46, 1177-1185.

Shiomi, Y., Nakanishi, S., Uehara, T., 2004. Characteristics of two-phase flow in a channel formed by chevron type plates. Exp. Therm. Fluid Sci. 28, 231-235.

Spedding, P.L., Woods, G.S., Raghunathan, R.S., Watterson, J.K., 1998. Vertical Two-Phase Flow: Part I: Flow Regimes. Chem. Eng. Res. Des. 76, 612-619.

Stephan, P., Martin, H., Kabelac, S., Mewes, D., Kind, M., Schaber, K., 2010. VDI Heat Atlas, 2nd Edition, Springer, Dusseldorf.

Thonon, B., Bontemps, A., 2002. Condensation of pure and mixture of hydrocarbons in a compact heat exchanger: experiments and modelling. Heat Transfer Engineering. 23, 3-17.

Thulukkanam, K., 2013. Heat Exchanger Design Handbook, 2nd Edition, Taylor & Francis Inc., Boca Raton, pp. 393-432.

Tribbe, C., Müller-Steinhagen, H. M., 2001a. Gas/Liquid Flow in Plate-and-Frame Heat Exchangers - Part I: Pressure drop measurements. Heat Transf. Eng. 22, 5-11.

Tribbe, C., Müller-Steinhagen, H. M., 2001b. Gas/Liquid Flow in Plate-and-Frame Heat Exchangers - Part II: Two-Phase Multiplier and Flow Pattern Analysis. Heat Transf. Eng. 22, 12-21.

Tsai, Y. C., Liu, F. B., Shen, P. T., 2009. Investigations of the pressure drop and flow distribution in a chevron-type plate heat exchanger. Int. Commun. Heat Mass Transf. 36, 574-578.

Vakili-Farahani, F., Amalfi, R.L., Thome, J.R., 2014a. Two-phase flow and boiling of R245fa in a 1 mm pressing depth plate heat exchanger. Part 1: Adiabatic pressure drop. Interfac. Phenom. Heat Transf. 2(4): 325-342.

Vakili-Farahani, F., Amalfi, R.L., Thome, J.R., 2014b. Two-phase flow and boiling of R245fa in a 1 mm pressing depth plate heat exchanger. Part 2: Flow boiling heat transfer. Interfac. Phenom. Heat Transf. 2(4): 343-361.

Vargaftik, N. B., Volkov, B. N., Voljak, L. D., 1983. International tables of the interfacial tension of water. J. Phys. Chem. Ref. Data. 12, 817-820.

Vlasogiannis, P., Karagiannis, G., Argyropoulos, P., Bontozoglou, V., 2002. Air water two-phase flow and heat transfer in a plate heat exchanger. Int. J. Multiph. Flow. 28, 757-772.

Wang, M., Infante Ferreira, C. A., 2017. Absorption heat pump cycles with NH3 – ionic liquid working pairs. Appl. Energy. 204, 819-830.

Wang, Z.Z., Zhao, Z.N., 1993. Analysis of performance of steam condensation heat transfer and pressure drop in plate condensers. Heat Transfer Engineering 14, 32–41.

Watson, E. L., Mckillop, A. A., Dunkley, W. L., Perry, R. L., 1960. (Plate Heat Exchangers) Flow Characteristics. J. Ind. Eng. Chem. 52, 733-740.

Webb, R.L., 1998. Convective condensation of superheated vapor. J. Heat Transfer. 120(2): 418-421.

Winkelmann, D., 2010. Condensation of pure refrigerants and their zeotropic mixtures in plate heat exchangers. Ph.D. thesis, Commissiariat à l'energie atomique (CEA).

Würfel, R., Ostrowski, N., 2004. Experimental investigations of heat transfer and pressure drop during the condensation process within plate heat exchangers of the herringbone-type. Int. J. Therm Sci. 43, 59-68.

Yan, Y.-Y., Lio, H.-C., Lin, T.-F., 1999. Condensation heat transfer and pressure drop of refrigerant R-134a in a plate heat exchanger. Int. J. Heat Mass Transf. 42, 993-1006.

List of figures

Fig. 7 – The separating lines between flow patterns reported in the different studies as function of mass flux and square root of the vapor quality. There appears to be an agreement for what concerns film flow. Other transitions differ between studies. The references listed in the legend are given in Table 1.

Fig. 8 - Flow pattern map of two-phase flow in PHEs, with dimensionless quantities on the x-axis ($Fr_{TP,\mathrm{ver}} / \Lambda^{0.5}$) and y-axis ($R_v^{0.5}$) (Tribbe and Müller-Steinhagen, 2001b; Vlasogiannis et al., 2002; Nilpueng and Wongwises, 2010; Winkelmann, 2010; Grabenstein and Kabelac, 2012; Grabenstein et al., 2017). Definitions of the dimensionless quantities are explained in Eqs. (24), (28) and (29). Separating lines are presented and the flow pattern descriptions are located in the zone. Corresponding studies are indicated in the legend by the reference numbers introduced in Table 1.

Fig. 9 – Simplified flow pattern map of two-phase flow in PHEs, which uses dimensionless quantities on the x-axis ($Fr_{TP,\mathrm{ver}} / \Lambda^{0.5}$) and y-axis ($R_v^{0.5}$). Separating lines between the flow patterns are included for the regular bubbly, irregular bubbly, slug, churn, film/partial film and transition between bubbly and film flow.

Fig. 10 - Flow pattern map of two-phase flow in PHEs, with dimensionless quantities on the x-axis (Re_L) and y-axis ($Fr_{TP,hor} / \Lambda^{0.5}$) (Tribbe and Müller-Steinhagen, 2001b; Vlasogiannis et al., 2002; Nilpueng and Wongwises, 2010; Winkelmann, 2010; Grabenstein and Kabelac, 2012, Grabenstein et al., 2017). The dimensionless quantities are introduced in Eqs. (23), (25) and (28). Separating lines are presented and the flow pattern descriptions are located in the zone. Corresponding studies are indicated in the legend by the reference numbers introduced in Table 1.

Fig. 11 – Simplified flow pattern map of two-phase flow in PHEs using dimensionless quantities on the x-axis (Re_L) and y-axis ($Fr_{TP,hor}/\Lambda^{0.5}$). Separating lines between the flow patterns are included for the regular bubbly, irregular bubbly, slug, churn, film, partial film and transition between bubbly and film flow.

Fig. 12 – Simplified flow pattern map of two-phase flow including lines for constant overall mass flux and constant vapor quality of R601 (pentane), which applies to the experiments reported by Sarraf et al. (2015a).

Fig. 13 – Comparison of flow pattern maps. The map of PHEs is compared with that of round mini tubes, which are based on the downward flow of air-water (Fukano and Kariyasaki, 1993; Mehta and Banerjee, 2014).

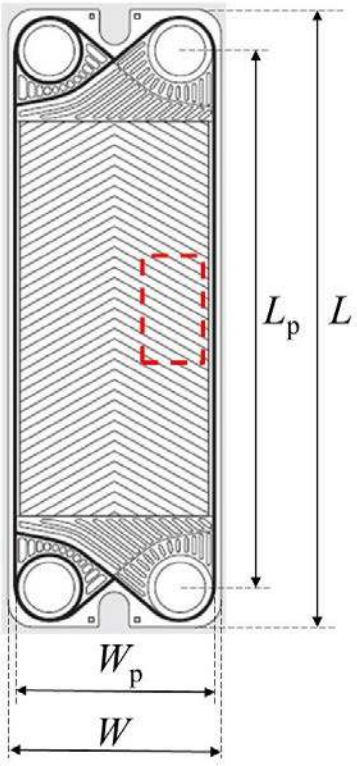

Fig. 1 - Representation of the heat exchanger plate with corrugation pattern indicating the overall plate width, W, the in gasket plate width, W_p, the overall plate length, L, and the port-to-port length, L_p.

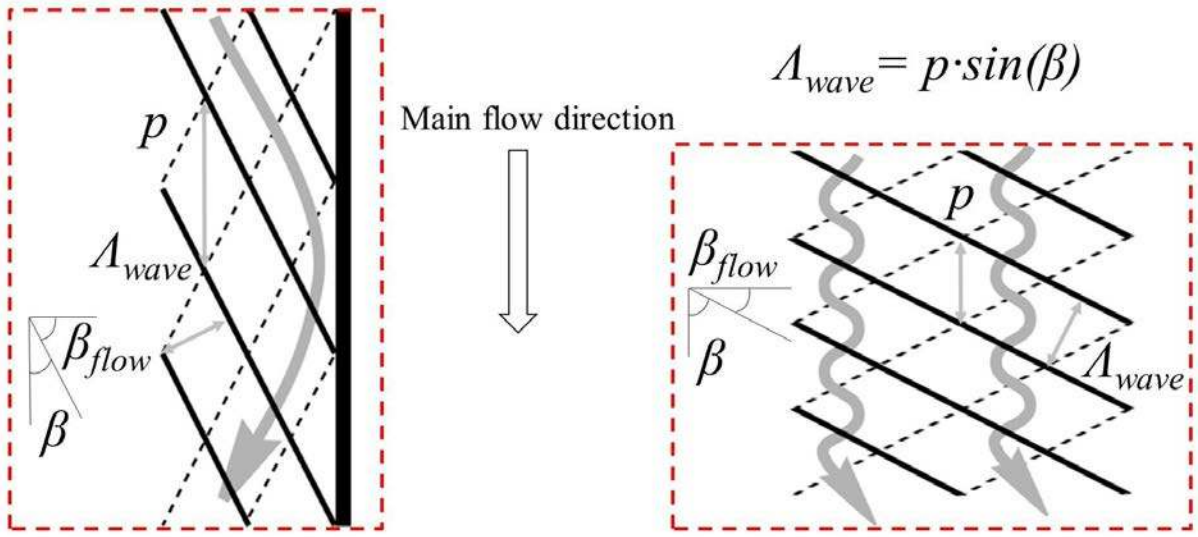

Fig. 2 - Representation of the corrugation profile including the corrugation pitch, p, the corrugation wavelength, Λ_{wave}, and the chevron angle, β; β_{flow} is the angle of the corrugation perpendicular to the flow direction; (left) small chevron angle, crossing flow and (right) large chevron angle, wavy longitudinal flow. Based on Winkelmann (2010).

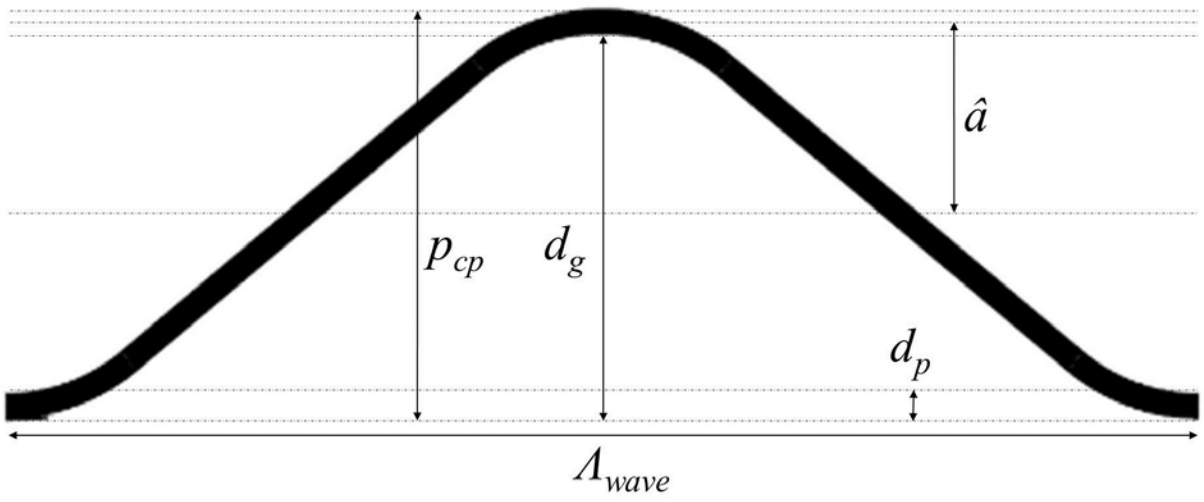

Fig. 3 - The relation between the compressed plate pitch, p_{cp}, the plate thickness, d_p, the channel gap, d_g, the corrugation amplitude, $\hat{a}$ and the corrugation wavelength, Λ_{wave}. Based on Winkelmann (2010).

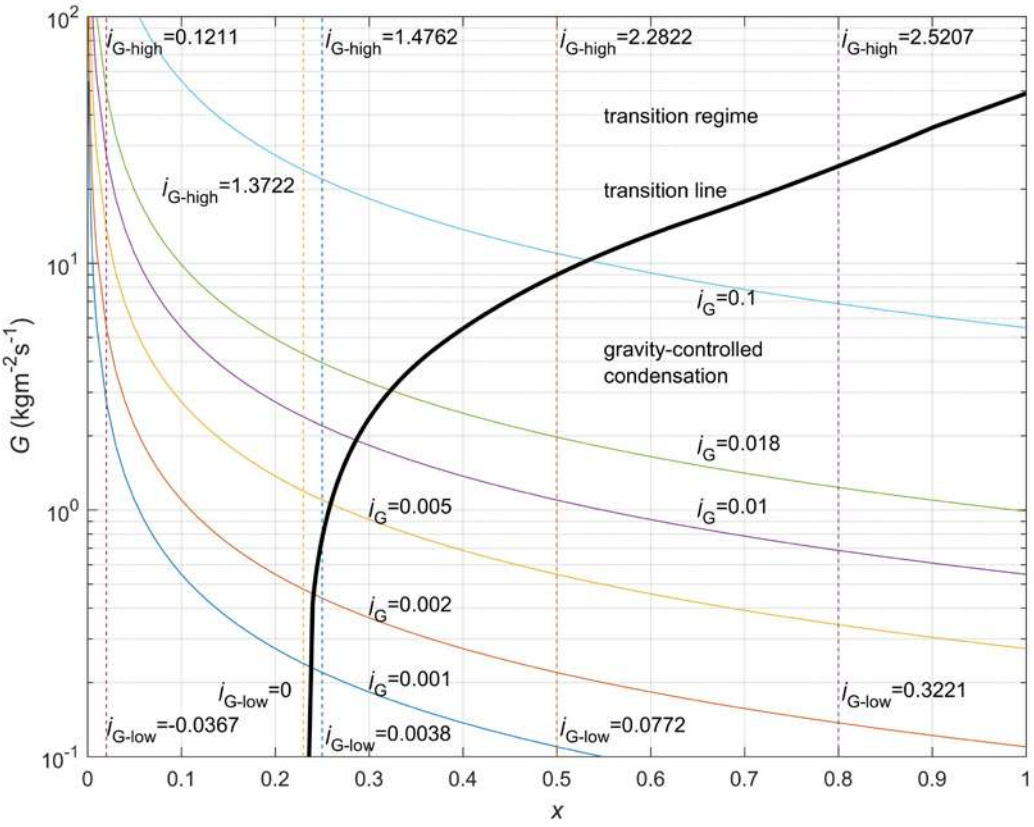

Fig. 4 - Transition of condensation mechanisms from gravity-controlled condensation to transition regime, which is in terms of vapor quality and mass flux for R32. Based on Mancin et al. (2013).

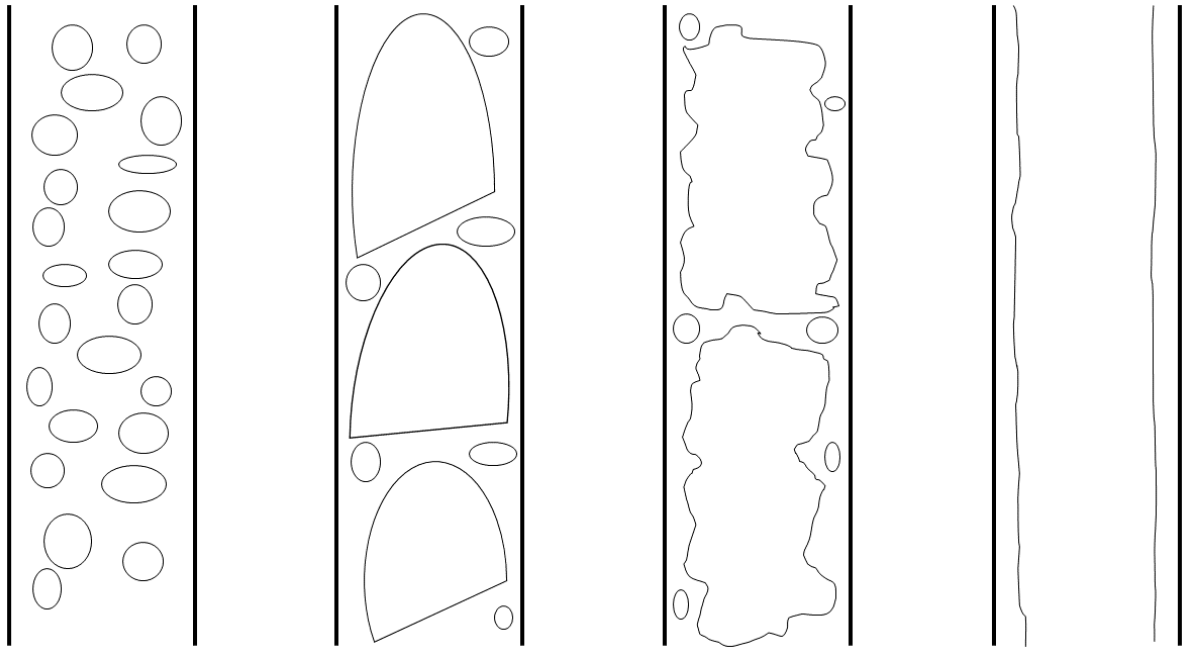

Fig. 5 - Representations of the four main flow patterns observed for downward two-phase flow in PHEs. From left to right: bubbly flow, slug flow, churn flow and film flow.

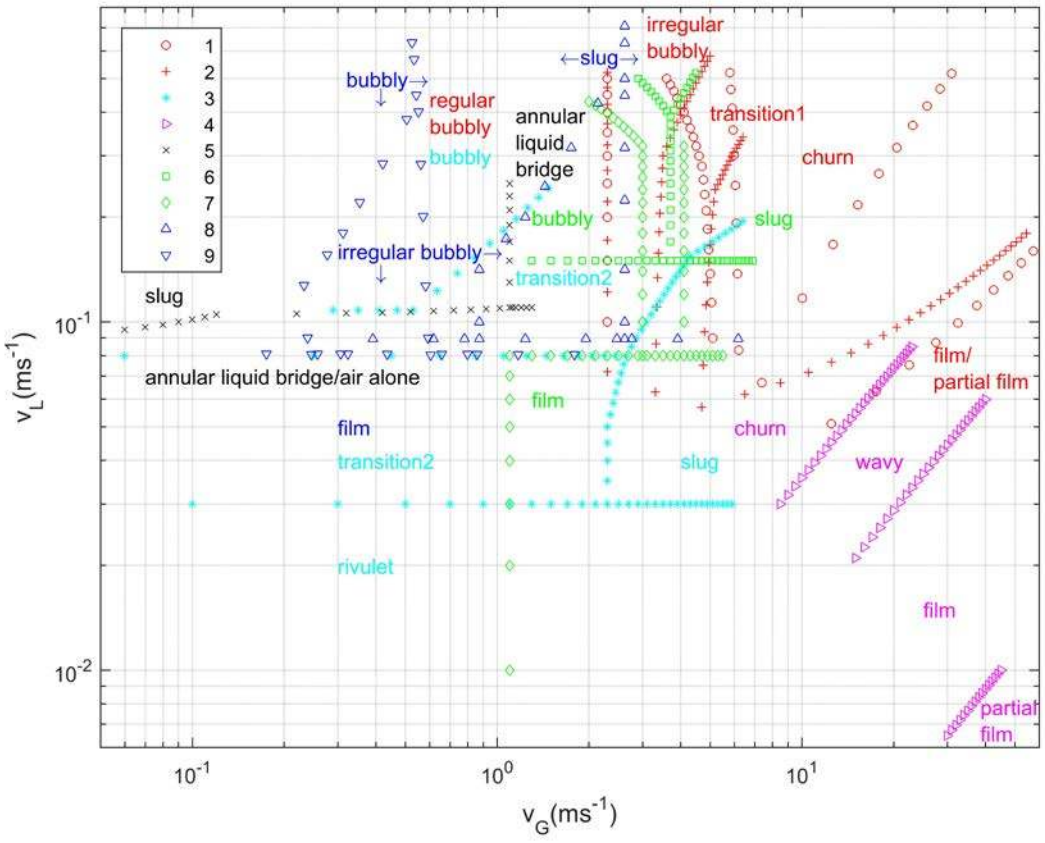

Fig. 6 - Flow pattern map of vertical downward two-phase flow in PHEs using logarithmic scales (Tribbe and Müller-Steinhagen, 2001b; Vlasogiannis et al., 2002; Nilpueng and Wongwises, 2010; Winkelmann, 2010; Grabenstein and Kabelac, 2012; Grabenstein et al., 2017). The superficial velocities of the vapor and liquid phases are used in the axes. Separating lines are presented and the flow pattern descriptions are located in the zone. Corresponding studies are indicated in the legend by reference numbers, which are listed in Table 1.

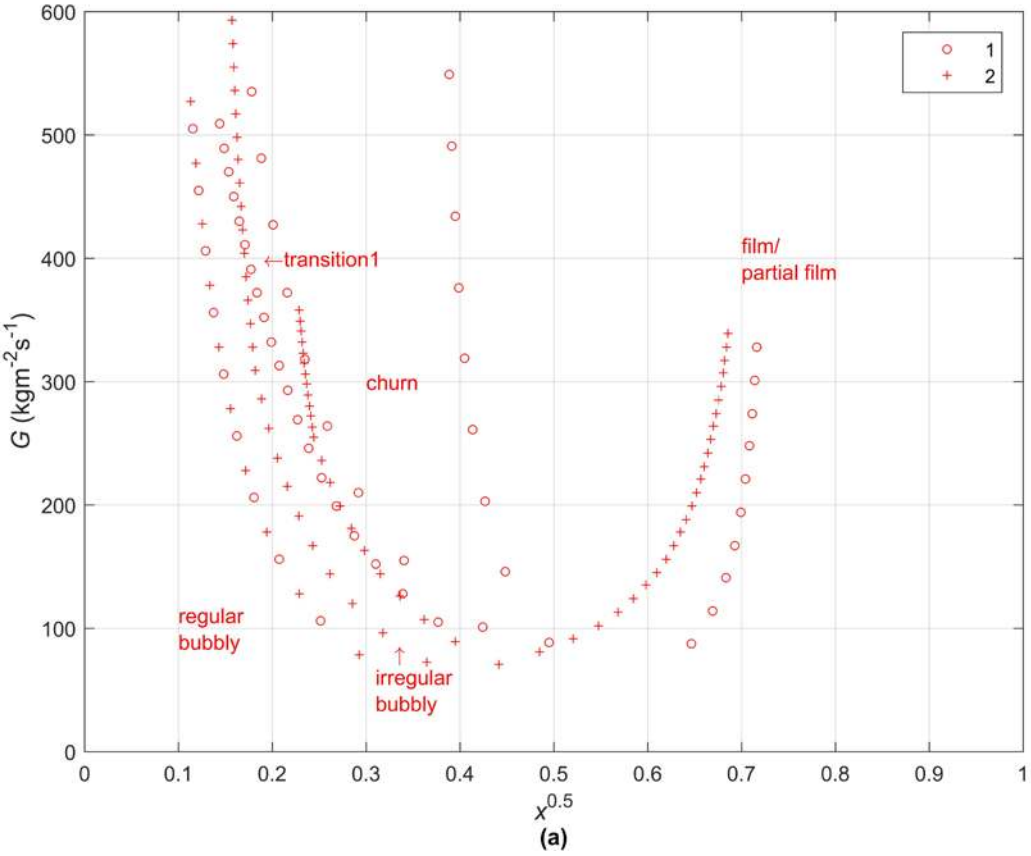
1
2
transition1
churn
film/
partial film
regular
bubbly
irregular
bubbly
G (kgm-2s-1)
x0.5
(a)

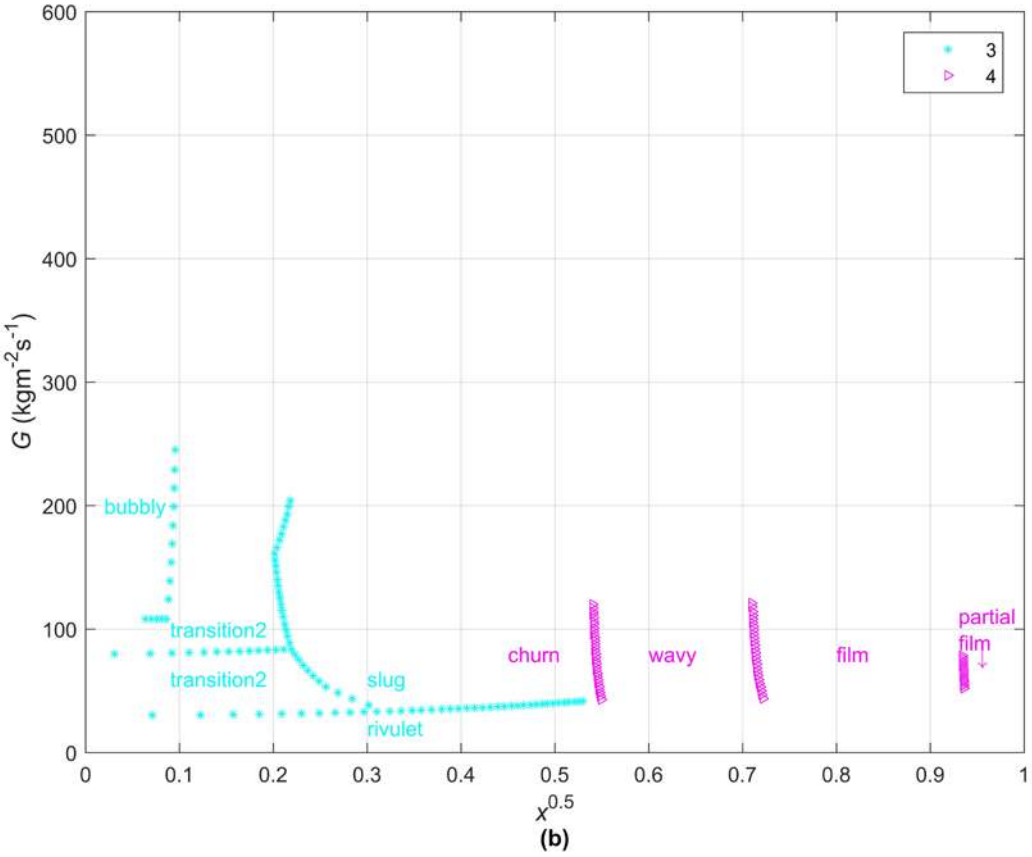
3
4
bubbly
transition2
transition2
slug
rivulet
churn
wavy
film
partial
film
G (kgm-2s-1)
x0.5
(b)

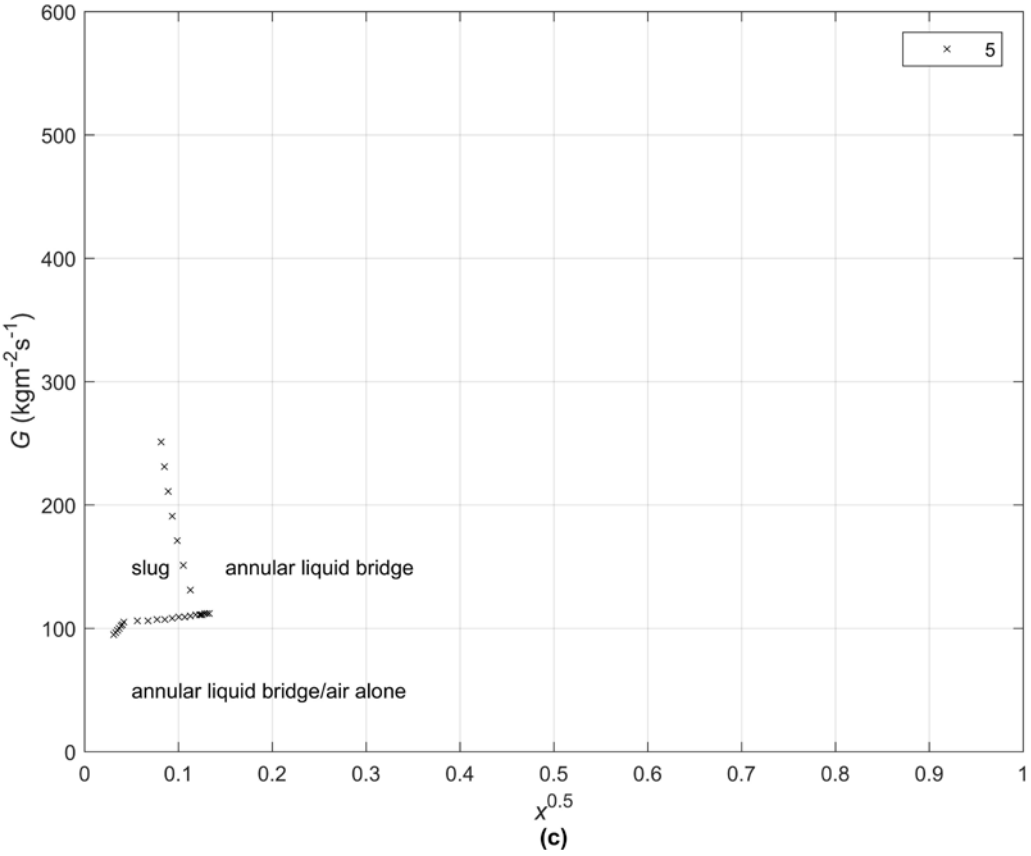
5
slug
annular liquid bridge
annular liquid bridge/air alone
G (kgm-2s-1)
x0.5
(c)

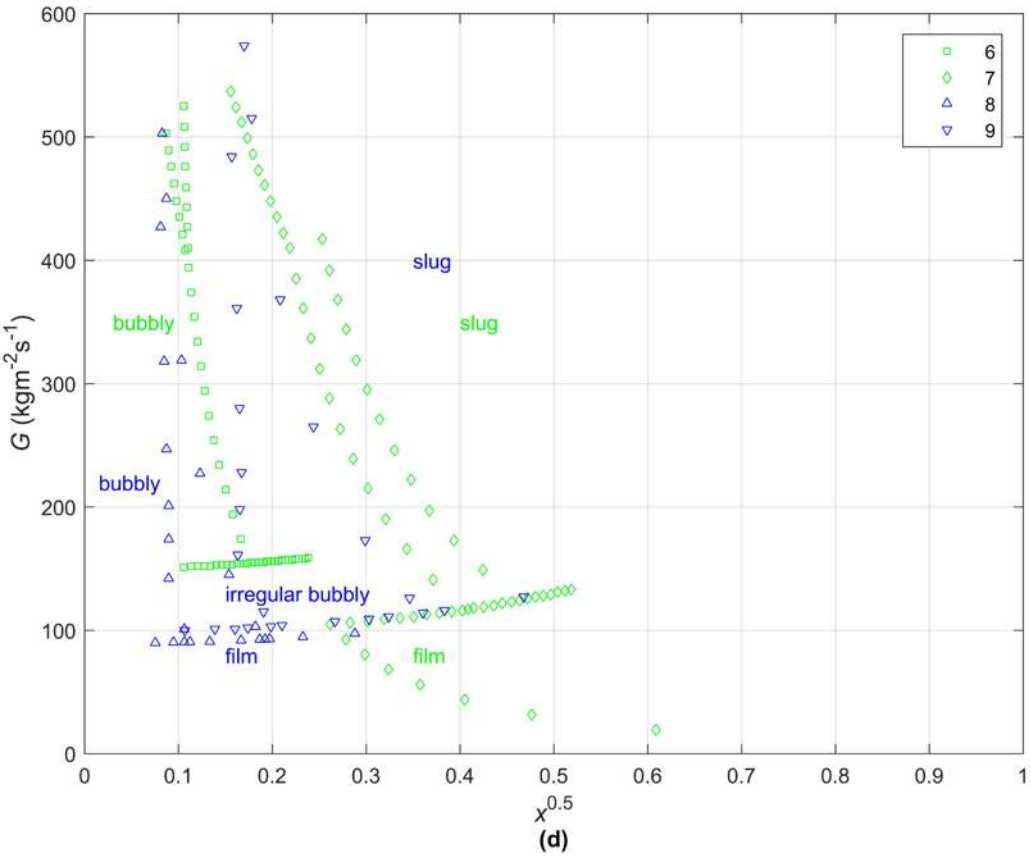
6
7
8
9
slug
bubbly
slug
bubbly
irregular bubbly
film
film
G (kgm-2s-1)
x0.5
(d)

Fig. 7 – The separating lines between flow patterns reported in the different studies as function of mass flux and square root of the vapor quality. There appears to be an agreement for what concerns film flow. Other transitions differ between studies. The references listed in the legend are given in Table 1.

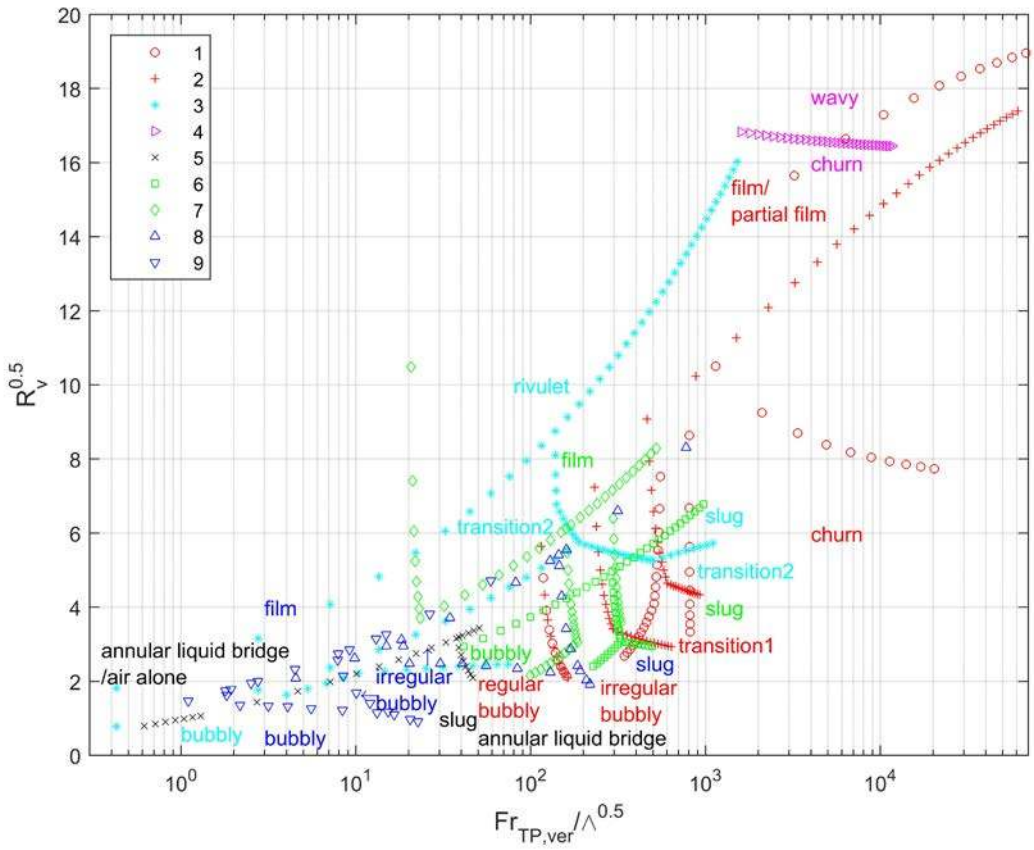

Fig. 8 - Flow pattern map of two-phase flow in PHEs, with dimensionless quantities on the x-axis ($Fr_{TP,\mathrm{ver}} / \Lambda^{0.5}$) and y-axis ($R_v^{0.5}$) (Tribbe and Müller-Steinhagen, 2001b; Vlasogiannis et al., 2002; Nilpueng and Wongwises, 2010; Winkelmann, 2010; Grabenstein and Kabelac, 2012; Grabenstein et al., 2017). Definitions of the dimensionless quantities are explained in Eqs. (24), (28) and (29). Separating lines are presented and the flow pattern descriptions are located in the zone. Corresponding studies are indicated in the legend by the reference numbers introduced in Table 1.

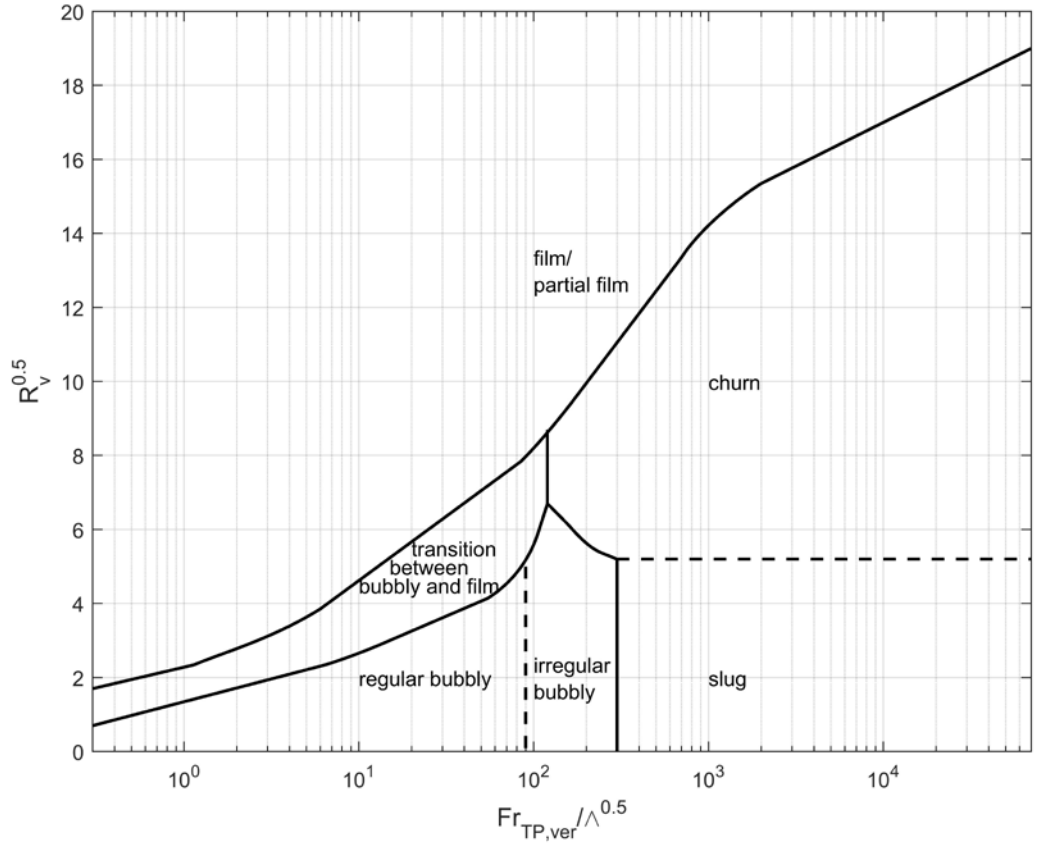

Fig. 9 – Simplified flow pattern map of two-phase flow in PHEs, which uses dimensionless quantities on the x-axis ($Fr_{TP,\mathrm{ver}} / \Lambda^{0.5}$) and y-axis ($R_v^{0.5}$). Separating lines between the flow patterns are included for the regular bubbly, irregular bubbly, slug, churn, film/partial film and transition between bubbly and film flow.

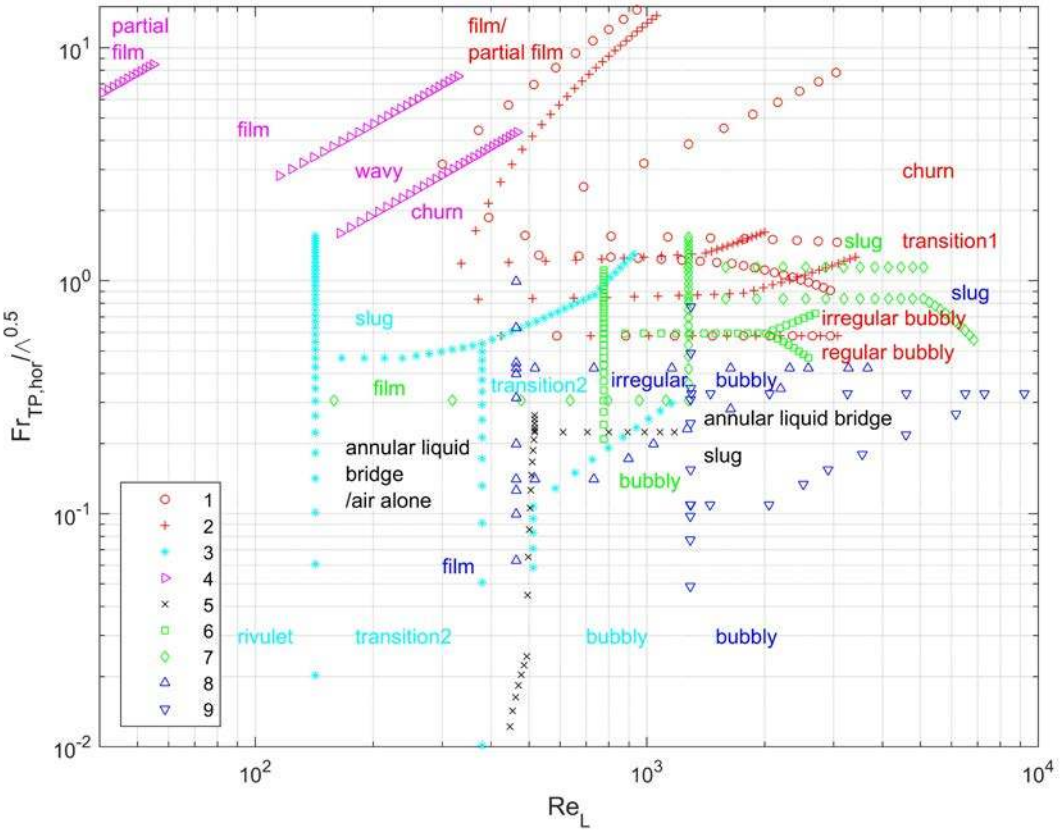

Fig. 10 - Flow pattern map of two-phase flow in PHEs, with dimensionless quantities on the x-axis (Re_L) and y-axis ($Fr_{TP,hor} / \Lambda^{0.5}$) (Tribbe and Müller-Steinhagen, 2001b; Vlasogiannis et al., 2002; Nilpueng and Wongwises, 2010; Winkelmann, 2010; Grabenstein and Kabelac, 2012, Grabenstein et al., 2017). The dimensionless quantities are introduced in Eqs. (23), (25) and (28). Separating lines are presented and the flow pattern descriptions are located in the zone. Corresponding studies are indicated in the legend by the reference numbers introduced in Table 1.

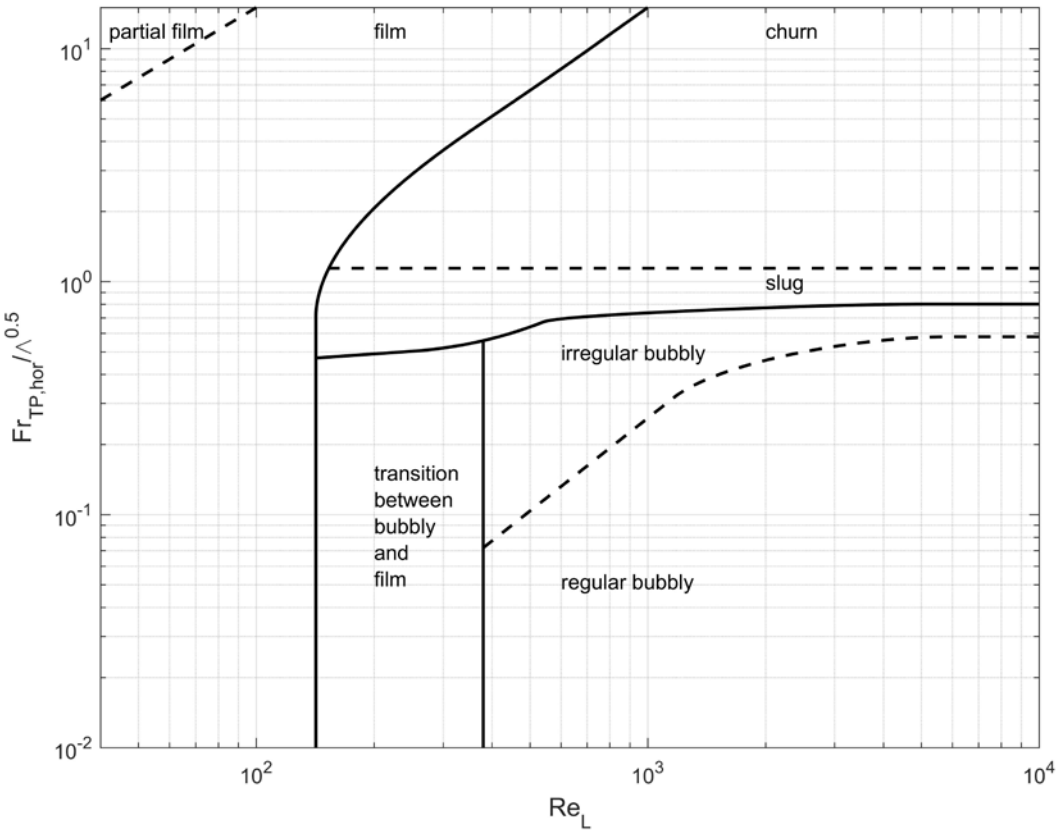

Fig. 11 – Simplified flow pattern map of two-phase flow in PHEs using dimensionless quantities on the x-axis (Re_L) and y-axis ($Fr_{TP,hor}/\Lambda^{0.5}$). Separating lines between the flow patterns are included for the regular bubbly, irregular bubbly, slug, churn, film, partial film and transition between bubbly and film flow.

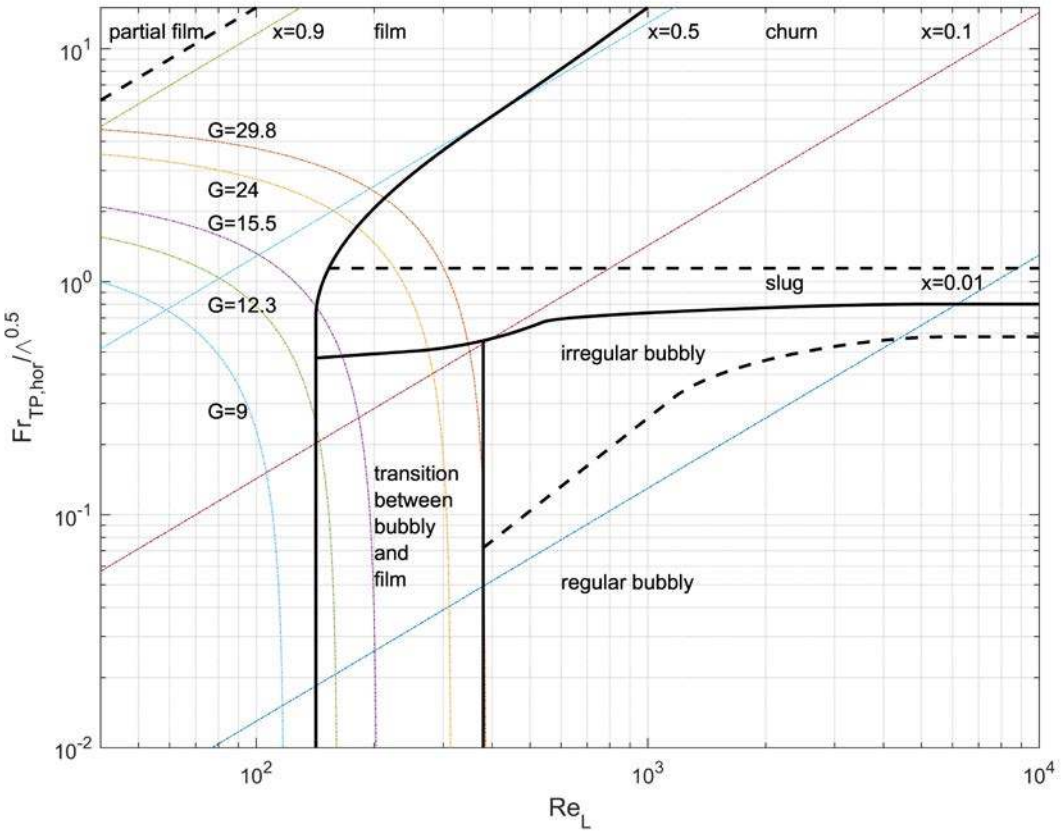

Fig. 12 – Simplified flow pattern map of two-phase flow including lines for constant overall mass flux and constant vapor quality of R601 (pentane), which applies to the experiments reported by Sarraf et al. (2015a).

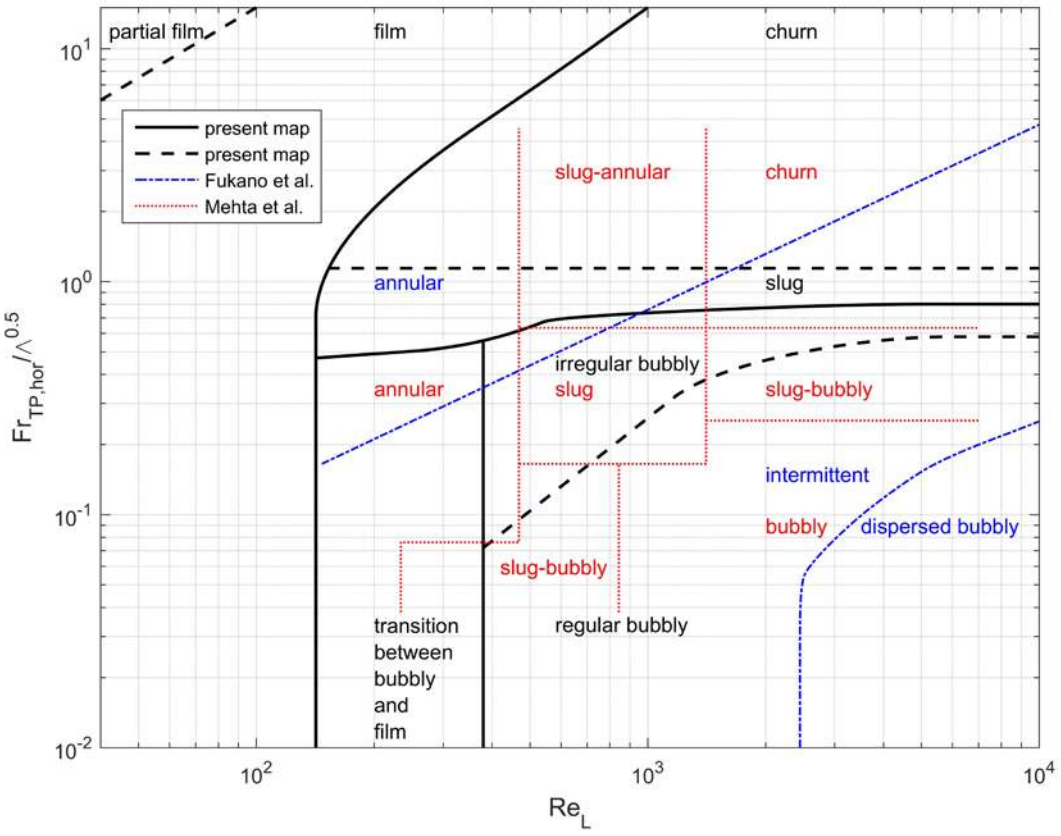

Fig. 13 – Comparison of flow pattern maps. The map of PHEs is compared with that of round mini tubes, which are based on the downward flow of air-water (Fukano and Kariyasaki, 1993; Mehta and Banerjee, 2014).

List of Tables

Table 1 – Comparison of geometric parameters used to develop heat transfer correlations.

Study	Enlargement factor Φ [-]	Chevron angle β [°]	Corrugation wavelength Λ_{wave} [mm]	Hydraulic diameter d_h [mm]	Equation multipliers [-]	Re_{eq} exponents [-]
Yan et al. (1999)	1.23	60	10.0	5.35	4.118	0.400
Han et al. (2003)	1.17	45	7.0	3.68	5.393	0.284
Han et al. (2003)	1.17	55	5.2	3.68	5.070	0.357
Han et al. (2003)	1.17	70	4.9	3.68	2.026	0.503
Longo et al. (2015)	1.24	65	8.0	3.23	2.325	0.445

Table 2 – List of flow patterns reported in visualization experiments.

Reference number	Study	Specific characteristics[1]	Flow patterns
1	Tribbe & Müller-Steinhagen (2001b)	β=30/30 β=30/60	Regular bubbly, irregular bubbly, transition between bubbly and churn[2], churn, film, partial film
2	Tribbe & Müller-Steinhagen (2001b)	β=60/60	Regular bubbly, irregular bubbly, transition between bubbly and churn[2], churn, film, partial film
3	Vlasogiannis et al. (2002)	-	Bubbly, transition between bubbly and rivulet[3], slug, rivulet
4	Winkelman (2010)	-	Churn, wavy, film, partial film
5	Nilpueng & Wongwises (2010)	-	Slug, annular liquid bridge, annular liquid bridge/air alone
6	Grabenstein & Kabelac (2012)	Air /Water	Bubbly, slug, film
7	Grabenstein & Kabelac (2012)	R365mfc	Bubbly, slug, film
8	Grabenstein et al. (2017)	Air /Water	Bubbly, irregular bubbly, slug, film
9	Grabenstein et al. (2017)	R365mfc	Bubbly, irregular bubbly, slug, film
10	Fukano & Kariyasaki (1993)	Round mini tube, d=4.9 mm	Dispersed bubbly, intermittent (elongated bubbly, slug, churn), annular
11	Mehta & Banerjee (2014)	Round mini tube, d=2.1 mm	Bubbly, slug -bubbly, slug, churn, slug-annular, annular

[1] Chevron angles or working fluids
[2] The transition between bubbly and churn is abbreviated as transition 1 in the following flow pattern maps
[3] The transition between bubbly and rivulet is abbreviated as transition 2 in the following flow pattern maps

Table 3 - Overview of the visualization experiments for two-phase vertical downward flow in PHEs.

Basic data					Fluids used		Plate materials	
Study	Model/type	Phase change	Pressure [bar]	Temperature [^{o}C]	Gas	Liquid	Main	Visualization
Tribbe et al. (2001a / b)	Alfa-Laval	No	2.5	25	Air	Water	Stainless steel	Polyester
Vlasogiannis et al. (2002)	Alfa-Laval P-01	No	1.3	25	Air	Water	Stainless steel	Plexiglas
Winkelman (2010)	Commercial[1]	No	1.3	25	Air	Water	Stainless steel	PMMA
Nilpueng & Wongwises (2010)	Commercial[1]	No	1.3	25	Air	Water	Stainless steel	Polyurethane
Grabenstein et al. (2012, 2017)	Industrial[1]	No	1.0	20	Air	Water	Stainless steel	Polyurethane
		No[2]	1.0	39.8	R365mfc	R365mfc	Stainless steel	Polyurethane

	Port-to-port plate	In gasket Plate	Corrugation dimensions [mm]					Enlargement
Study	length, L_p[mm]	width, W_p[mm]	Channel gap, d_g	Plate thickness, d_p	Amplitude, $\hat{a}$	Λ_{wave}	d_h	factor, ϕ
Tribbe et al. (2001a / b)	640	210	3	0.5	1.5	12	5.26	1.14
Vlasogiannis et al. (2002)	352	100	2.4	0.6	1.2	10	4.24	1.13
Winkelman (2010)	400	160	3	0.6	1.5	9.3	4.90	1.22
Nilpueng & Wongwises (2010)	635	100	2.5	0.5	1.25	8.5	4.20	1.19
Grabenstein et al. (2012, 2017)	408	388	3	0.5	1.5	11.4	5.19	1.16

	Corrugation structure		Flow area,	Chevron angle, β [°][3]		Distributor type	
Study	Main	Profile	A_f [cm^2]	Symmetrical	Unsymmetrical	Mixing section	Inlet area
Tribbe et al. (2001a / b)	Chevron	Sinusoidal	6.3	30/30, 60/60	30 / 60	Single section	Triangular
Vlasogiannis et al. (2002)	Chevron	Sinusoidal	2.4	60/60		Single section	Triangular
Winkelman (2010)	Chevron	Sinusoidal	4.8	25.7/25.7		Single section	Triangular
Nilpueng & Wongwises (2010)	Chevron	Sinusoidal	2.5		35/80	Single section	Triangular
Grabenstein et al. (2012, 2017)	Double chevron	Sinusoidal	11.6	63/63/63/63[4], 27/27/27/27[4]		Eight sections	Rectangular

[1] Commercial / Industrial refers to the width of the plates, the industrial plates being wider.
[2] The PHE is adiabatic but the refrigerant is heated before the inlet to achieve the desired vapor quality
[3] The structure is symmetrical for combination of the same chevron angles, and unsymmetrical for combination of different chevron angles
[4] Double chevron structure is composed of four chevron angles

Table 4 – Fluid property comparison of air-water and refrigerants in the visualization experiments and the condensation experiments.

	T_{sat}	ρ_G	ρ_L	μ_G	μ_L	Δh_{LG}	σ	λ_L	Pr_L
units	℃	$kg \cdot m^{-3}$	$kg \cdot m^{-3}$	μPa·s	μPa·s	$kJ \cdot kg^{-1}$	$mN \cdot m^{-1}$	$W \cdot m^{-1}$	-
Air/water (2.5 bar, 25 ℃)	-	2.92	997	18.47	890.0	-	72.0	0.607	6.13
Air/water (1.3 bar, 25 ℃)	-	1.52	997	18.45	890.0	-	72.0	0.607	6.13
Air/water (1.0 bar, 20 ℃)	-	1.19	998	18.21	1001.6	-	72.8	0.599	7.00
R365mfc (1.0 bar)	39.8	5.96	1225	9.93	409.8	188	13.4	0.081	7.08
R32 (22.7 bar)	36.4	66.05	910	13.56	99.3	246	5.0	0.117	1.77
R601 (1.03 bar)	36.5	3.02	609	7.22	357.2	357	14.2	0.107	4.38